photonics

MDPI

Article

Detection of Atmospheric Wind Speed by Lidar Based on Quadrichannel Mach–Zehnder Interferometer

Jun Li [1,*], Yusheng Lu [1,*], Haima Yang [1,2], Zeng Li [3], Jin Liu [4], Jia Qiang [2] and Yuwei Chen [5]

[1] School of Optical-Electrical and Computer Engineering, University of Shanghai for Science and Technology, Shanghai 200093, China
[2] Key Laboratory of Space Active Opto-Electronics Technology, Shanghai Institute of Technical Physics, Chinese Academy of Sciences, Shanghai 200083, China
[3] Shanghai Yihao Testing Technology Co., Ltd., Shanghai 201802, China
[4] School of Electronic and Electrical Engineering, Shanghai University of Engineering Science, Shanghai 201620, China
[5] Advanced Laser Technology Lab of Anhui Province, Hefei 230039, China
* Correspondence: lijuny@usst.edu.cn (J.L.); 203590767@st.usst.edu.cn (Y.L.)

Abstract: For a long time, wind speed profile measurement has been the primary task of weather forecasting. Therefore, the detection of atmospheric wind speed is extremely important for studying the changes in atmospheric motion. In order to solve the problems of insufficient data collection, low resolution, and low accuracy in atmospheric wind field detection, this paper introduces the relevant theories of wind speed detection, completes the optical design of the system according to the research objectives, and determines the selection of optical devices. At the same time, a Doppler wind lidar system based on a quadrichannel Mach–Zehnder interferometer is designed and built to carry out ground-based observation experiments, collect echo signal data, and inverse the atmospheric radial wind speed. Furthermore, the wind measurement error is analyzed. Firstly, the paper introduces the basic principle of the wind measurement system, i.e., using the Doppler effect of light, and then analyzes the frequency discrimination device of the system in detail, and obtains the theoretical calculation method of atmospheric wind speed inversion. At the same time, the relevant datasets of wind measurement system are analyzed, including backscattering ratio, aerosol, and molecular extinction coefficient, and the emission mechanism of the large pulse laser is also studied in detail, which provides a theoretical basis for the model construction of Doppler lidar and the research on the enhancement of pulsed laser emission energy. Secondly, according to the research index of wind measurement, a Doppler wind measurement lidar system based on a quadrichannel Mach–Zehnder interferometer is designed, including the design of ab external light path transceiver system, internal light path interferometer, software and hardware, and algorithm. The calibration of the quadrichannel Mach–Zehnder interferometer is completed, with its maximum interference contrast reaching 0.869. Through the self-developed optical transceiver system and data acquisition system, the echo signal of lidar is received and detected. Lastly, the data of echo signals collected by the interferometer are analyzed, the radial atmospheric wind speed profile is inversed, and the signal-to-noise ratio and wind speed measurement error of the system are evaluated. The experimental results show that the maximum signal-to-noise ratio (SNR) of the system can reach 1433 when the emission pulse energy of the large pulse laser is adjusted to 255 mJ, and the farthest wind speed detection distance is about 8 km. The high-precision wind speed detection range can reach 2 km, the actual wind measurement errors in this range are all within 1.593 m/s, and the minimum error is only 0.418 m/s. In addition, the backscattering coefficient and extinction coefficient of atmospheric molecules and aerosols in the range of 8 km and the atmospheric temperature in the range of 10 km are also measured. The measurement accuracy of the aerosol extinction coefficient is $\pm 0.001\ \mathrm{m}^{-1}$, and the measurement error of atmospheric temperature within 10 km is within 2 K, achieving the expected goals.

Keywords: atmospheric wind speed; Mach–Zehnder interferometer; Doppler lidar

check for updates

Citation: Li, J.; Lu, Y.; Yang, H.; Li, Z.; Liu, J.; Qiang, J.; Chen, Y. Detection of Atmospheric Wind Speed by Lidar Based on Quadrichannel Mach–Zehnder Interferometer. *Photonics* **2023**, *10*, 726. https://doi.org/10.3390/photonics10070726

Received: 25 March 2023
Revised: 17 June 2023
Accepted: 21 June 2023
Published: 25 June 2023

1. Introduction

Wind observation is the key input of weather and air quality forecasting models. However, the observation results in existing global wind networks with the greatest influence on numerical weather prediction are limited to the ground profile (such as airborne sensors and radiosonde profiles), the near-surface layer (such as sea surface wind), or limited layer measurement (such as atmospheric motion vector wind and aircraft sensors over the ocean) [1]. Vertical resolution wind profile measurement has always been listed as one of the biggest gaps in observation data, such as the OSCAR database of the World Meteorological Organization (WMO). This gap is particularly obvious in the ocean and Southern Hemisphere, and alternative satellite remote sensing measurement is needed to fill this gap.

Doppler wind lidar (DWL) can remotely measure the range-resolved wind speed projected on the instrument line of sight (LOS) by emitting laser and measuring the frequency change of atmospheric backscattered light (i.e., Doppler frequency shift) [2]. In recent years, due to the demand for improved and increasingly localized wind measurement and weather forecast (e.g., in the field of renewable energy) and the availability of reliable laser sources, electronic equipment, and optical equipment (including optical fibers and laser optical coatings), the DWL field has developed rapidly. With the commercial ground wind lidar system becoming more and more accessible, the use and understanding of DWLs system and the integration of wind products are also increasing.

Through the verification of ground observation, the double-edge Fabry–Pérot interferometer can effectively derive the wind profile from the long-span vertical atmospheric molecular scattering signal. As early as 1999, the European Space Agency (ESA) chose the direct detection technology for the space atmospheric dynamics project (ADM-Aeolus). ADM-Aeolus was successfully launched in 2018. Since then, the technical problems of lidar were solved, and the first global tropospheric wind profile was obtained from space. The simulation and real-time assimilation of horizontal wind information confirmed that the project still has room for further improvement, verifying the concept of space single-beam lidar. Therefore, a more potential follow-up instrument should be operated to consolidate the achievements obtained from the ADM Aeolus mission, and the original configuration of the instrument (single-beam ultraviolet emission lidar) should be kept as much as possible. By replacing Fizeau and Fabry–Pérot interferometers with a unique four-channel Mach–Zehnder (QMZ) interferometer, the concept of the receiver can be re-examined, which may relax the operating parameters of the system, expand the observation ability, and invert the radiation characteristics of airborne clouds. The ability to obtain wind profile and cloud/aerosol radiation characteristics meets the requirements of meteorological forecasting institutions on atmospheric dynamics and radiation, which are the two highest priorities. The vertical distribution of atmospheric aerosol and the atmospheric wind field formed by its movement are very important for studying the Earth’s climate environment.

In the wind energy industry, the Doppler LiDAR technique provides a promising alternative to in situ techniques in wind energy assessment, turbine wake analysis and turbine control. Doppler LiDARs have also been applied in meteorological studies, such as observing boundary layers and tracking tropical cyclones. These applications demonstrate the capability of Doppler LiDARs for measuring backscatter coefficients and wind profiles. Doppler LiDAR measurements show considerable potential for validating and improving numerical models [3]. In addition, wind profile light detection and ranging (LiDAR) is an important tool for observing features within the atmospheric boundary layer [4].

At present, the remote sensing technology of backscattering lidar has been used to deduce the boundary layer and extinction of aerosol and cloud. In this case, the inversion of cloud and aerosol optical parameters needs to clean the air or use the assumption about backscattering and extinction ratio. As determined in the early stage of lidar development, hyperspectral resolution lidar (HSRL) technology allows to distinguish between molecular and particle scattering, as well as more accurately characterize the extinction and backscattering coefficients of aerosols or clouds. The advantage of high-spectral-resolution lidar is that it does not need to separate the input of molecules and aerosol particle scattering. Many HSRL systems have developed filtering technology to separate aerosol scattering with narrow spectrum from molecular scattering echo with wider spectrum by using an iodine molecular absorption cell and Michelson or Fabry–Pérot interferometer (FPI). All these systems operate in direct detection (measuring backscattered light power), which has the advantage of relying on particle and molecular scattering, while allowing the expansion of range and function. Direct detection technology has been selected for space observation of wind or aerosol and cloud using an ultraviolet Fabry–Pérot interferometer UV-FPI (ESA EarthCare mission). However, in any case, all HSRL technologies developed so far need to emit quasi-monochromatic light, i.e., using a single-mode laser, and usually need to inject seeds. In addition, most systems require precise frequency locking of the transmitter with respect to the filter. These requirements lead to complex transmitter design involving a precise servo loop and may become a fault point in space applications. In contrast, a four-channel Mach–Zehnder interferometer can work with a multimode laser [5]. The optical path difference (OPD) of QMZ is matched with the free spectral range (FSR) of laser, so that the interference states of all laser modes are exactly the same. Instead of separating molecular and particle signals in two different channels, QMZ determines the interference contrast given by backscattered light. Regardless of the spectral positioning of the laser frequency relative to the transfer function of QMZ, the contrast is clearly determined by the signals given by four detection channels with orthogonal phases. In this way, neither the laser nor the interferometer needs frequency stability.

This paper describes the calibration of a four-channel Mach–Zehnder interferometer, enabling wind speed inversion and error analysis of Doppler lidar in atmospheric wind speed measurement.

2. Working Principle

2.1. QMZ Frequency Discrimination Principle

Compared with the classic Mach–Zehnder interferometer (MZI), the main notable feature is that a quarter-wave plate (QWP) is introduced into one arm of the interferometer to introduce extra phase difference (π/2 of one polarization direction relative to the other). Assuming that no other polarization-dependent path differences occur, QMZ provides four output signals with orthogonal phases. The two classical MZI output channels are separated by a polarizer oriented along one axis of QWP and detected by four non-imaging detectors [6–9]. In order to work with multimode laser, the optical path difference, Δ, of QMZ must match the free spectral range FSR of the laser:

$$\Delta = \frac{c}{FSR} \tag{1}$$

where C is the speed of light in vacuum. In this case, the interference state at the QMZ output remains unchanged regardless of the laser mode.

According to Equation (1), the intensity fraction transmitted through the polarizer is equal, and the signal transmitted by each channel (from 1 to 4) is written as

$$S_i = \frac{S_t}{4} a_i [1 + M_i M_a \sin(\varphi + (i-1)\frac{\pi}{2})] \tag{2}$$

where S_t is the total signal, a_i is the relative photometric sensitivity of channel I, M_i is the instrument interference contrast of channel I, M_a is the interference contrast given by atmospheric backscattering signal, and φ is the interference phase. According to Equation (2), the complex signal Q is calculated as

$$Q = Q_2 + iQ_1 \tag{3}$$

$$\begin{aligned} Q_1 &= \frac{a_3 S_1 - a_1 S_3}{a_3 M_3 S_1 + a_1 M_1 S_3} \\ Q_2 &= \frac{a_4 S_2 - a_2 S_4}{a_4 M_4 S_2 + a_2 M_2 S_4} \end{aligned} \quad (4)$$

The interference contrast given by atmospheric backscattering signal is the modulus of complex signal Q:

$$M_a = |Q| \quad (5)$$

According to Equation (1), the atmospheric backscattering spectrum is a convolution of the emission spectrum and spectrum broadening caused by random motion of molecules and particles. Therefore, the atmospheric contrast M_a can be expressed as

$$M_a = \frac{\beta_p}{\beta_p + \beta_m} M_p + \frac{\beta_m}{\beta_p + \beta_m} M_m \quad (6)$$

where β_p and β_m are the backscattering coefficients of particles and molecules, respectively, and M_p and M_m are the interference contrast given by the backscattering coefficients of particles and molecules, respectively. The interference contrast $\delta\nu$ given by the full width at half maximum (FWHM) source of the spectrum is expressed as follows according to Equation (2):

$$M = \exp\left[-\left(\frac{\pi \delta v \Delta}{2c\sqrt{\ln(2)}} \right)^2 \right] \quad (7)$$

On one hand, the spectrum of particle backscattering is broadened by the spectrum of wind turbulence in the detection volume, and most of the time it can be ignored (the radial velocity of 1 $m \cdot s^{-1}$ corresponds to 4 MHz broadening at 532 nm). The particle scattering spectrum, like the laser spectrum, is a comb composed of relatively narrow spectral lines. The response of the laser-matched interferometer to this spectrum is exactly the same as that of a typical FWHM ($\delta\nu \approx 200$ mHz) single line, and the interference modulation M_p is ≈ 0.8. On the other hand, due to the wide molecular velocity distribution, the spectral broadening of molecular backscattering signal is much larger (about 1 GHz). Convolution with a typical 1 GHz FSR transmission frequency comb produces an almost constant spectrum continuum without interference modulation ($M_m \approx 0$). Therefore, the obtained contrast is equal to the instrument contrast generated by the laser source itself, and the retrieved contrast M_a is equal to

$$M_a = R_p M_p \quad (8)$$

where R_p can be expressed as the backscattering ratio of particles, and β_m and β_p are the backscattering coefficients of molecules and particles, respectively.

$$R_p = \frac{\beta_p}{\beta_p + \beta_m} \quad (9)$$

In addition to the comparison, the interference phase of the output signal is obtained by the independent variable of the complex signal Q:

$$\varphi = \arg(Q) = \frac{2\pi\Delta}{\lambda_0}(1 + \frac{2V_{LOS}}{c}) \quad (10)$$

where λ_0 is the emission wavelength, and VLOS is the wind speed. From the interference phase information, the frequency of the backscattered signal can be inverted, and the Doppler frequency shift can be obtained.

The calibration of QMZ is based on the measurement of two instrument parameters: a_i and M_i. These measurements can be performed internally through the reference channel, including collecting a small amount of light from the laser source. In the process of atmospheric measurement, complex signals are averaged in multiple laser emissions to improve the measurement accuracy. Since the interference phase may change during this period, the reference signal is still recorded to perform phase compensation summation to avoid any underestimation of contrast. For a series of N signals, we get

$$R_p = \frac{\beta_p}{\beta_p + \beta_m} = \frac{\sum_{i=1}^{N} |Q_i/Q_{Ri}|}{N} \tag{11}$$

Therefore, the wind speed VLOS(See Appendix A.1.) is deduced as

$$V_{LOS} = \frac{c\lambda_0}{4\pi\Delta} \arg\left(\sum_{i=1}^{N} Q_i/Q_{Ri}\right) \tag{12}$$

where Q_R is the reference complex signal.

2.2. Performance Evaluation of Doppler Wind Lidar

Since there are molecules and particles in the atmosphere, the power-normalized spectrum of the lidar atmospheric echo signal is a linear combination of the power-normalized scattering spectrum of molecular I_m and particle I_p, which can be written as

$$I_a = \frac{1}{R_\beta} I_m + \frac{R_\beta - 1}{R_\beta} I_p \tag{13}$$

where R_β is the backscattering ratio, and the two spectra of the scattered signal excited by monochromatic laser have different shapes because they have gone through different processes. However, due to the use of a pulsed laser source limited by Fourier transform, it can be assumed that the spectrum generated by the scattering of laser light by molecules and particles has Gaussian distribution in frequency; then,

$$I_x(\sigma') = \frac{1}{\gamma_x \sqrt{\pi}} \exp\left[-\frac{(\delta' - \delta)^2}{\gamma_x^2}\right] \tag{14}$$

where γ_x is the half width at 1/e of the distribution. In addition, according to Equation (15), the center wave number σ of the received signal is Doppler-shifted compared with the center wave number σ_0 of the transmitted signal.

$$\sigma = \sigma_0 \leq (1 + 2V/c) \tag{15}$$

where V is the average radial velocity of the scattering volume. In fact, the backscattering intensity spectrum I_m from molecules is the convolution of the emitted laser energy spectrum and the Gaussian Doppler spectrum generated by the molecular thermal velocity distribution (ignoring the influence of Raman scattering and Brillouin scattering), and the half-peak width at 1/e of the given Gaussian Doppler spectrum density is $\gamma_{u,mol}$, i.e.,

$$\gamma_{u,mol} = \frac{2\sigma_0}{c}\sqrt{\frac{2kT}{m}} \tag{16}$$

where k is the Boltzmann constant, T is the temperature of scattering medium (atmosphere), m is the average mass of atmospheric molecules, and $V_{u,mol} = (2\ kT/m)^{1/2}$ is the most probable rate of thermal motion of molecules. The half-peak width at 1/e of the maximum Rayleigh backscattering power spectrum of atmospheric molecules is

$$\gamma_m = \left(\gamma_e{}^2 + \gamma_{u,mol}{}^2\right)^{1/2} \tag{17}$$

where γ_e is the line width of the transmitted pulse, and c is the speed of light.

On the one hand, for the temperature T = 250 K, $v_{u,mol} \approx 380\ m\cdot s^{-1}$; that is, for the emission wavelength $\lambda_1 = 1/\sigma_1$ = 532 nm, $\gamma_{u,mol} \approx 4.8 \times 10^{-2}\ cm^{-1}$ (1.4 GHz), and, for λ_2 = 355 nm, $v_{u,mol} \approx 7.1 \times 10^{-2}\ cm^{-1}$(2.1 GHz). On the other hand, injecting seed light source into the Nd:YAG solid-state laser can emit a single-frequency pulse with a near Fourier-transform limit. For a typical pulse duration of 20 ns, the Fourier-transform limited pulse corresponds to a spectral width of about $\gamma_e \approx 1.67 \times 10^{-3}\ cm^{-1}$(50 MHz). Therefore, compared with Rayleigh broadening of atmospheric molecules, we can ignore the width of emitted light(See Appendix A.2.) and write

$$\gamma_m \approx \gamma_{u,mol} = \frac{2\sigma}{c}\sqrt{\frac{2kT}{m}} \tag{18}$$

The backscattered signal I_p from aerosol particles is broadened by the wind turbulence spectrum in the detected volume unit, assuming a Gaussian line shape, and the 1/e half-width of the maximum Brownian motion power spectrum of particles is $\gamma_{u,part}$. Similarly, the half-peak width at 1/e of the obtained aerosol particle backscattering spectrum is written as

$$\gamma_p = \left(\gamma_e{}^2 + \gamma_{u,part}{}^2\right)^{1/2} \tag{19}$$

Considering that the velocity of aerosol particles is about several meters per second, and that, for λ_2 = 532 nm, the radial velocity of 1 $m\cdot s^{-1}$ corresponds to a Doppler frequency shift of $1.3 \times 10^{-4}\ cm^{-1}$, the particle backscattering spectrum is defined as the first approximation of the laser source spectrum. The spectral linewidth of the particle scattering signal can be 50–100 times smaller than that of the molecular scattering signal, as shown in Figure 1 [10–12].

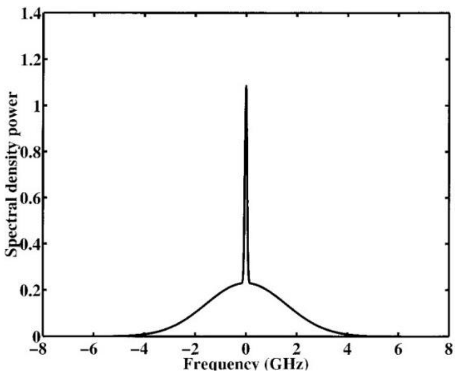

Figure 1. Normalized spectrum energy distribution diagram of atmospheric signals.

Measurements are made during the day, but noisy detectors are also taken into account, which means that background signals are generally superimposed on lidar signals. When the signal is processed, the level of the background signal is measured and subtracted from the actual signal. In addition, it is assumed that the measurement of background light is carried out through a large number of time averages; hence, compared with the error of lidar signal, its error can be ignored. Therefore, before any data processing, the background level can be subtracted from the recorded signal without obvious additional error. For simplicity, the background signal is not considered in the equation below describing the measurement principle, and the existence of background light leads to the reduction in signal-to-noise ratio. Let N_A be the average signal photon number and N_B be the average background photon number, where η is the detection efficiency. Then,

$$SNR = \sqrt{\left(\frac{\eta N_A}{1 + N_B/N_A}\right)} \tag{20}$$

Assuming $a_i = M_i = 1 (i = 1\sim4)$, the variance of Q_1 can be expressed as

$$\frac{\mathrm{var}(Q_1)}{\overline{Q}_1^2} \approx \frac{\mathrm{var}(S_1 - S_2)}{\left(\overline{S}_1 - \overline{S}_2\right)^2} + \frac{\mathrm{var}(S_1 + S_2)}{\left(\overline{S}_1 + \overline{S}_2\right)^2} - 2\frac{\mathrm{cov}(S_1 - S_2, S_1 + S_2)}{\left(\overline{S}_1 - \overline{S}_2\right)\left(\overline{S}_1 + \overline{S}_2\right)} \tag{21}$$

where $\overline{x}$ and var(x) represent the mean and variance of x, respectively, and cov(x,y) represents the covariance of x and y. The average value of Q_1 is given by the following formula:

$$\overline{Q}_1 \approx \frac{\overline{S}_1 - \overline{S}_2}{\overline{S}_1 + \overline{S}_2} \tag{22}$$

Furthermore, it is assumed that the noises on S_1 and S_2 are uncorrelated with each other. That is, only considering the detection noise, there are

$$\mathrm{var}(S_1 - S_2) = \mathrm{var}(S_1 + S_2) = \mathrm{var}(S_1) + \mathrm{var}(S_2) \tag{23}$$

$$\mathrm{cov}(S_1 - S_2, S_1 + S_2) = \mathrm{var}(S_1) - \mathrm{var}(S_2) \tag{24}$$

Then, it can be inferred that

$$\mathrm{var}(Q_1) \approx \left(1 + \overline{Q}_1^2\right) \frac{\mathrm{var}(S_1) + \mathrm{var}(S_2)}{\left(\overline{S}_1 + \overline{S}_2\right)^2} - 2\overline{Q}_1 \frac{\mathrm{var}(S_1) - \mathrm{var}(S_2)}{\left(\overline{S}_1 + \overline{S}_2\right)^2} \tag{25}$$

Next, suppose that the signal detection after adding background noise is limited by shot noise, i.e., $\mathrm{var}(S_1) + \mathrm{var}(S_2) = \eta(N_{A1} + N_{B1})$, and $\mathrm{var}(S_1)$-$\mathrm{var}(S_2) = \eta\overline{Q_1}N_{A1}$. Then, the variance of Q_1 is given by

$$\mathrm{var}(Q_1) \approx \frac{1 + F_{B1}\overline{Q}_1^2}{SNR_1{}^2} \tag{26}$$

$F_{B1} = (N_{B1} - N_{A1})/(N_{B1} + N_{A1})$, which is a numerical value varying between -1 and 1, and the specific numerical value depend on the number of background photons. For the calculation of the standard deviation of Q_2, the same expression can be obtained according to the calculation steps of Equations (21)–(25).

Q_S is defined as the arithmetic square root of Q_1 square plus Q_2 square:

$$Q_S = \sqrt{Q_1{}^2 + Q_2{}^2} \tag{27}$$

Since the signals Q_1 and Q_2 are uncorrelated, there are

$$\mathrm{var}(Q_S) \approx \frac{\overline{Q}_1^2 \mathrm{var}(Q_1) + \overline{Q}_2^2 \mathrm{var}(Q_2)}{\overline{Q}_1^2 + \overline{Q}_2^2} \tag{28}$$

If approximate treatment is carried out according to Equation (26), with $N_{A1} = N_{A2} = N_{A/2}$ and $N_{B1} = N_{B2} = N_{B/2}$ (i.e., the transmission of the two polarizations is equal), there are $SNR_1 = SNR_2 = SNR/\sqrt{2}$ and $F_{B1} = F_{B2} = F_B$. Then, the final variance of Q_S is given by

$$\mathrm{var}(Q_S) \approx \frac{2}{SNR^2}\left(1 + F_B \frac{\overline{Q}_1^4 + \overline{Q}_2^4}{\overline{Q}_1^2 + \overline{Q}_2^2}\right) \tag{29}$$

According to Equation (15), the interference phase φ can be written as $\varphi = \varphi_0 + \delta_\varphi$, where

$$\varphi_0 = 2\pi l \sigma_0, \delta_\varphi = \frac{4\pi\sigma_0 l V}{c} \tag{30}$$

According to Equation (2), $Q_1 = M_a\sin\varphi$, $Q_2 = M_a\cos\varphi$, and $\varphi = \arctan(Q_1/Q_2)$. Derived from Equation (6), $R_\beta = (M_p\text{-}M_m)/(M_p\text{-}Q_S)$. Then, from Equations (4) and (26), it is deduced that

$$\begin{aligned} \overline{Q}_1^2 + \overline{Q}_2^2 &= M_a^2 \\ \overline{Q}_1^4 + \overline{Q}_2^4 &= M_a^4\left[1 - \tfrac{1}{2}\sin^2(2\varphi)\right] \end{aligned} \tag{31}$$

Finally, combined with the above equation, the standard deviation of R_β is obtained as follows:

$$\varepsilon_{R_\beta} = \frac{R_\beta^2}{M_p - M_m}[\mathrm{var}(Q_s)]^{1/2} \approx \frac{\sqrt{2}}{SNR}\frac{R_\beta^2}{M_p - M_m}\left\{1 + F_B M_a^2\left[1 - \frac{1}{2}\sin^2(2\varphi)\right]\right\}^{1/2} \tag{32}$$

In order to calculate the error of wind speed V, the variance of R_Q must be determined. Since the noise coefficients of Q_1 and Q_2 are uncorrelated, the variance of R_Q is

$$\mathrm{var}(R_Q) \approx \overline{R}_Q^2\left[\frac{\mathrm{var}(Q_1)}{\overline{Q}_1^2} + \frac{\mathrm{var}(Q_2)}{\overline{Q}_2^2}\right] \approx \frac{\overline{Q}_1^2}{\overline{Q}_2^2}\left(\frac{1 + F_{B1}\overline{Q}_1^2}{\overline{Q}_1^2 SNR_1^2} + \frac{1 + F_{B2}\overline{Q}_2^2}{\overline{Q}_2^2 SNR_2^2}\right) \tag{33}$$

Substituting Equations (4) and (30) into the above formula, it is concluded that

$$\mathrm{var}(R_Q) \approx \frac{2}{SNR^2}\frac{1}{M_a^2\cos^4\varphi}\left[1 + \frac{1}{2}F_B M_a^2\sin^2(2\varphi)\right] \tag{34}$$

Then, the standard deviation of ε_φ is

$$\varepsilon_\varphi = \frac{[\mathrm{var}(R_Q)]^{1/2}}{dR_Q/d\varphi} = \frac{\sqrt{2}}{SNRM_a}\left[1 + \frac{1}{2}F_B M_a^2\sin^2(2\varphi)\right]^{1/2} \tag{35}$$

If the signal-to-noise ratio is high, the reference measurement error can be ignored. Combined with $R_\beta = (M_p - M_m)/(M_p - Q_S)$, the standard deviation of radial wind speed measurement(See Appendix A.3.) can finally be obtained as follows [13–16]:

$$\varepsilon_V \approx \frac{c}{4\pi\sigma_0 l}\frac{\sqrt{2}}{SNRM_a}\left[1 + \frac{1}{2}F_B M_a^2\sin^2(2\varphi)\right]^{1/2} \tag{36}$$

3. Lidar Design

3.1. General Architecture

The overall arrangement of lidar based on the four-channel Mach–Zehnder interferometer is shown in Figure 2. The aperture of a Newton telescope is only 150 mm, so that it can be installed on satellite detectors or ground stations. In order to experience small optical path difference, the optical path difference designed inside the interferometer is only 3 cm. Since the experimental wind speed measurement needs to compare the atmospheric signal with the interference phase of the reference pulse emitted by the laser, a small number of emitted light beams are collected and sent into the integrating sphere through one of the beam splitters, and the optical fiber is connected to the output port of the integrating sphere. The integrating sphere ensures that the whole emitted pulse is collected, as well as the distribution or arrangement of possible small changes in intensity space. The laser, beam expander, beam splitter, and integrating sphere are installed on one side of the telescope structure. The other side is equipped with receiving optics, filter, and a signal optical fiber connector. In order to avoid any deviation caused by mechanical deformation, only one input port of QMZ is used in this experiment. The sampled signal and the collected echo signal are connected to a fiber coupler (95% for outputting echo signal and 5% for outputting sampled signal), and their outputs are connected to the QMZ input port. Because the output fiber of the experiment is short, it cannot ensure good mode mixing and good beam depolarization; thus, the mode scrambler can be inserted into the output of the fiber coupler before being injected into the interferometer. Four avalanche photodiodes and differential amplifiers (AD8138) used to detect the interferometer output signals ensure the detection accuracy of the signals, and the signals are collected by 16 bit, 25 MHz, and 104 mW analog-to-digital converters (LTC2271).

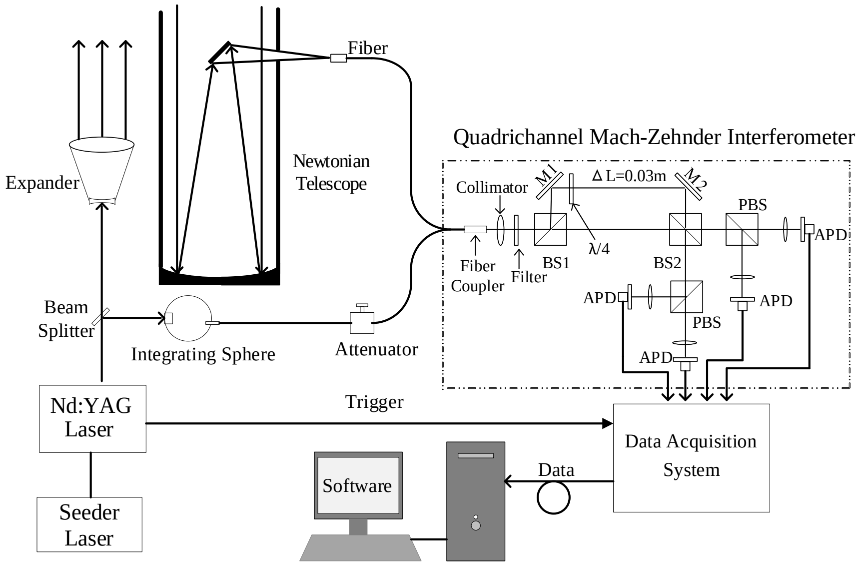

(**a**)

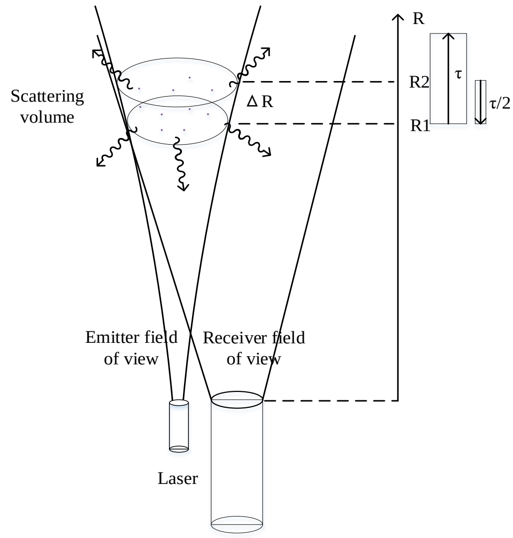

(**b**)

Figure 2. General layout of lidar: (**a**) design of lidar; (**b**) illustration of the lidar geometry.

Figure 2b shows the optical transmission schematic diagram of the laser radar (the figure shows an off-axis transceiver system, which is a coaxial transceiver system when the transmitted beam is in the geometric center of the receiving telescope). In the figure, the transmitting laser emits a Gaussian beam into the atmosphere. At time t + τ, the optical signal is highly scattered by R2 (R2 = c(t + τ)/2), whereby ΔR = R1 − R2 =cτ/2, which is the length of the scattered gas at this moment, and cτ/2 is called the effective pulse space length. In order to ensure that the telescope can receive the complete backscattered echo signal of the transmitted Gaussian beam, it is usually necessary to make the receiving field angle of the telescope more than twice that of the laser; however, if the ratio is too large, it will receive too much sky background light, and, if it is too small, there will be a “blind area” where the optical signal cannot be received at low altitude. Above a certain height, the telescope field of view completely contains the emission field of view, which is called the "full area", and the transition area is between "blind area" and "full area".

The simplest form of lidar equation is

$$P(R) = KG(R)\beta(R)T(R) \quad (37)$$

where P(R) is the received optical power at R, k is the factor representing the performance of lidar, G(R) is the geometric factor, β(R) is the backscattering coefficient at R, which is a parameter to measure the ability of the atmosphere to scatter the emitted light in a certain direction, and T(R) represents the attenuation of laser by atmospheric transmittance. In Equation (37), the system factor k can be written as

$$K = P_0 \frac{c\tau}{2} A\eta \quad (38)$$

where P_0 is the average power of a single laser pulse, A is the area in the scatterer when the telescope observes the scattered gas, and η is the optical efficiency of the system.

The geometric factor G(R) is

$$G(R) = \frac{O(R)}{R^2} \quad (39)$$

where O(R) is the overlapping function of the transmitted beam and the received field of view. In Figure 2b, the overlapping function has a value of 0 in the blind area, 1 in the full area, and 0–1 in the transition area.

The internal design of a large pulse laser is shown in Figure 3.

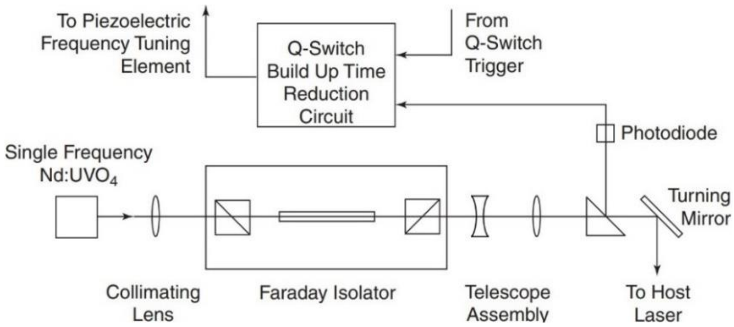

Figure 3. Internal design of large pulse laser.

In this figure, Nd:YVO_4 is a single-chip and single-frequency seed laser source, and its output wavelength is 1.064 μm, which is the same as that of Nd:YAG. Nd:YVO_4 can work at a single frequency because the diode pump light is strongly absorbed in an end mirror of a monolithic cavity. The first mode that reaches the threshold in the monolithic cavity is the mode closest to the peak of the gain curve of Nd:YVO_4. When the pump power is absorbed within a short distance from the end mirror, the first mode introduces a population inversion density to clamp the gain to a threshold level. Because all other modes in the cavity have a common spatial node on the end mirror, these modes obtain the same population inversion density [17]. Other modes with smaller stimulation emission cross-sections cannot reach the threshold. Before the second mode reaches the threshold, the laser can usually run above the threshold. In addition, Nd:YVO_4 is pumped by a single stripe laser diode, which is set slightly off-axis to prevent feedback to the diode. Because the output of laser diode is sensitive to temperature, its output wavelength is controlled by a TE cooler. The temperature of single Nd:YVO_4 is also controlled by a TE cooler. This makes it possible to scan the wavelength output of single Nd:YVO_4 by changing its temperature. Figure 4 is a schematic diagram of a laser source composed of Nd:YVO_4.

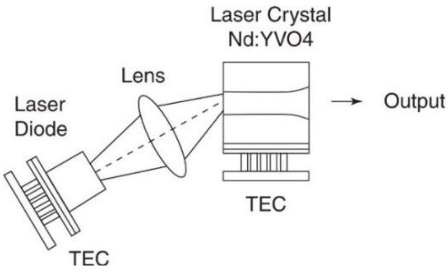

Figure 4. Nd:YVO_4 single-frequency laser source.

Second, in the internal design of the large pulse laser, the collimator lens is added to ensure that the beam with small diameter and good collimation passes through the Faraday isolator to obtain the maximum output and isolation. There are two important reasons for adding Faraday isolator: one is to prevent any backward radiation from the host laser from damaging the seed laser; the other is to decouple the seed laser resonator from the host resonator to maintain the frequency stability of the seed laser. In order to maintain the frequency stability of the seed laser, it is necessary to decouple the two resonators, which puts strict requirements on the extinction ratio of Faraday isolator [18]. For the high-gain laser designed by the seed laser, the extinction ratio must reach 30 dB. Adding lens assembly is helpful to optimize the spatial mode matching between the seed laser and the host, which prolongs the lifetime of the seed laser photons in the host resonator and increases the power of the seed laser coupled into the host cavity.

Figure 5 is the system block diagram of the main engine of 6350 large pulse laser and related components of PRO/Lab/GCR series laser.

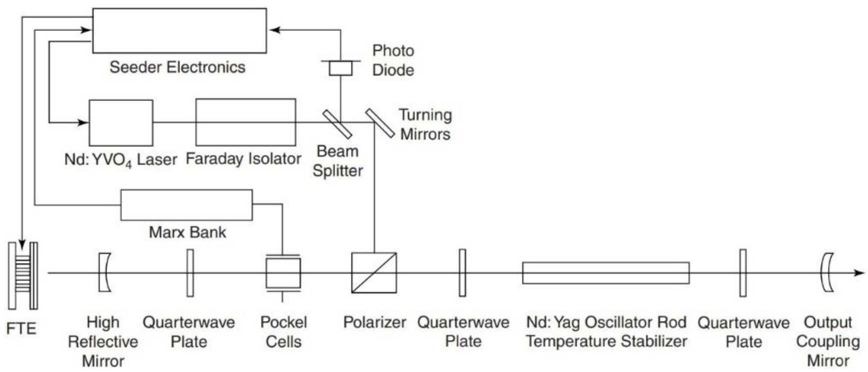

Figure 5. Design drawing of connection between 6350 large pulse laser and host computer.

The steering mirror is added to guide the beam and keep the seed laser beam aligned with the optical axis of the host. Two mirror surfaces are connected with the bottom plate of the seeder, and one mirror surface is connected with the GCR series optical guide rail. At the same time, the mirror is adjustable to keep the optical alignment of the seeder beam [19–22]. The temperature control and power supply circuit provide temperature control for the temperature-sensitive optical components in the large pulse laser to ensure stable performance. Temperature-stable components include a laser diode pumping source that keeps its output emission frequency within the absorption bandwidth of Nd:YVO_4 and another that controls the output frequency of the seed laser Nd:YVO_4 seed laser crystal. In addition, the Q-switch establishes a tuning minimization circuit (signal processor), the purpose of which is to minimize the setup time of the Q-switch and keep the optimal frequency overlap between the seed laser and the host laser. The temperature stability of internal cooling water in the design block diagram is provided by the combination of the temperature sensor and proportional valve, which keeps the Nd:YAG oscillator rod at an average temperature, thus fixing the gain curve envelope of its frequency. The device regulates the flow of external cooling water in the heat exchanger and keeps the internal cooling water at a uniform temperature, while the pressure sensor ensures the existence of external cooling water pressure. A quarter-wave plate for suppressing space hole burning is included on each side of the Nd:YAG oscillator rod to suppress space hole burning. The piezoelectric frequency tuning element is a movable PRO/Lab/GCR series high reflector, which is used to keep the optimal frequency coincident with the seed laser.

In addition, the design should also include devices to eliminate all secondary plasma effects and prevent unnecessary reflection from any optical surface. Even the reflection on the surface of the antireflective coating directly on the shaft is enough to form a weak plasma. Because the laser is temperature-tuned, it can identify the frequency of the seed laser in an unknown way. Such a plasma effect can be significant enough to have a significant impact on the implanted seeds. Table 1 shows the design parameters of 6350 large pulse laser.

Table 1. Design parameters of 6350 large pulse laser.

Design Indicators	Parameters
Nominal wavelength	1064 nm
Output power	3.0 mW ± 15%
Monopulse energy	1200 mJ
Spatial model	>70% Gaussian correlation coefficient (at 1 m)
Beam diameter	9 mm
Divergence angle	0.4 mrad
Pulse duration	20 ns
Energy stability between pulses	±1%
Frequency width	<0.003 cm^{-1}
Frequency modulation	<±10 MHZ
Warmup time	15 min
Optimum operating temperature	22 °C

3.2. QMZ Design

The schematic diagram of the four-channel Mach–Zehnder interferometer (QMZ) is shown in Figure 6.

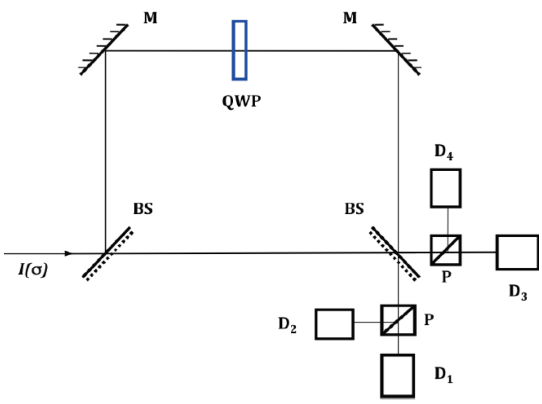

Figure 6. Quadrichannel Mach–Zehnder configuration: M, mirror; BS, beam splitter; QWP, quarter-wave plate; D1, D2, D3, D4, detectors.

In the above figure, the signal collected by the external optical transceiver system is sent to the collimator through the optical fiber, and the optical fiber collimator is pre-aligned to collimate the light emitted from the FC/PC connector optical fiber and has the performance of diffraction limit. The optical fiber collimator has no moving parts, which is compact in structure and convenient to be integrated into existing devices [23]. Considering that the light emitted from the optical fiber has a Gaussian intensity distribution, the divergence angle can be estimated using Equation formula (37).

$$\theta \approx \left(\frac{D}{f}\right)\left(\frac{180}{\pi}\right) \tag{40}$$

where θ is the divergence angle, d is the simulated diameter (MFD), and f is the focal length of the collimator. This formula is suitable for a single-mode fiber, but it will underestimate the divergence angle of a multimode fiber, because the light emitted from the fiber does not have a Gaussian intensity distribution. For light with different wave bands, the divergence angle curve is shown in Figure 7.

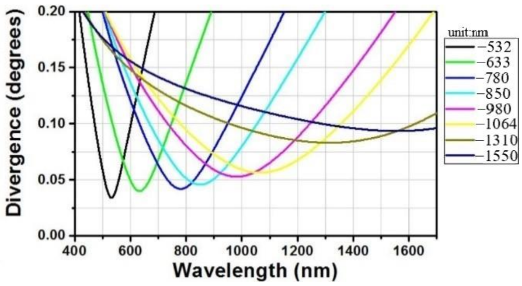

Figure 7. Divergence angle curve.

After that, the echo of 532 nm needs to pass through the filter to eliminate the influence of interference on other bands such as 1064 nm, before finally passing through a four-channel Mach–Zehnder interferometer with short optical path difference, and then being collected by the lens and sent to the detector.

For the interferometer with 532 nm band, the nonpolarized beam-splitting cube with a beam-splitting ratio of 50:50 is used as the beam-splitting mirror in this experiment, and the response band is between 400 and 700 nm, with a size of 1 inch [24]. Similarly, for the interferometer using a 1064 nm band, the beam splitter is an unpolarized beam splitter cube with a beam splitting ratio of 50:50, and the response band is between 700 and 1100 nm, with a size of 1 inch. Their design indicators are shown in Table 2.

Table 2. Cube design indicators.

Design Index	Parameter
The side length of the cube	1″(25.4 mm)
Transparent aperture	>20.3 × 20.3 mm
Wave front error of transmission	$<\lambda/4$
Transmitted beam deviation	≤5 arcmin
Damage threshold	0.25 J/cm^2

The reflectivity and transmittance of the beam-splitting cube using 532 nm band are shown in Figure 8.

As can be seen from the above figure, the reflectivity of the wavelength of 532 nm in the beam splitting cube is between 40% and 50%, and the transmittance is between 50% and 60%.

The reflectivity and transmittance of the beam-splitting cube using the 1064 nm band are shown in Figure 9.

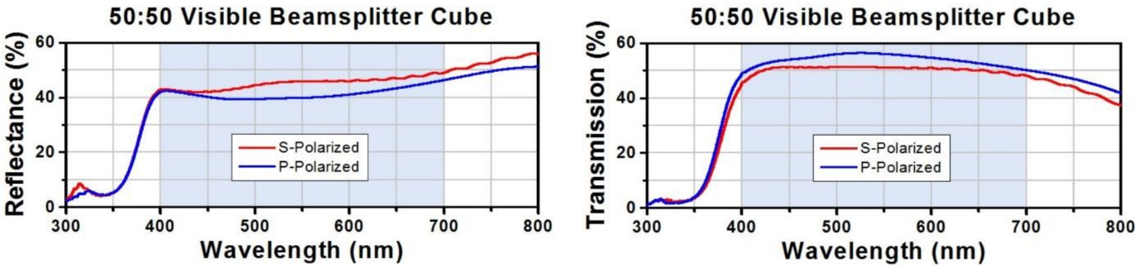

(**a**) (**b**)

Figure 8. Reflectance and transmittance of beam-splitting cube in 532 nm band: (**a**) reflectance curve in 532 nm band; (**b**) transmittance curve of 532 nm band.

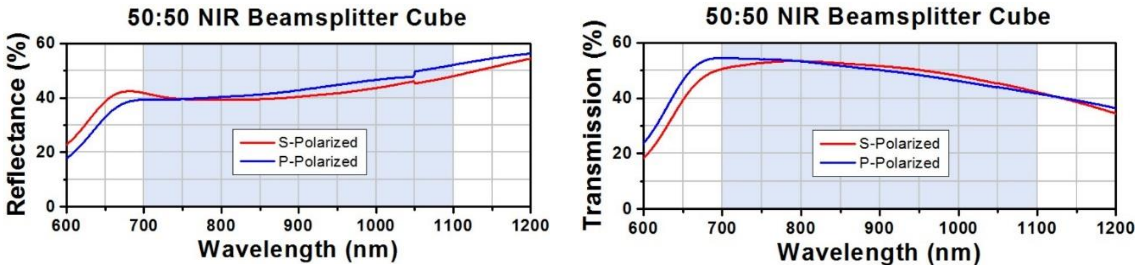

(**a**) (**b**)

Figure 9. Reflectance and transmittance of beam splitting cube in 1064 nm band: (**a**) reflectance curve in 1064 nm band; (**b**) transmittance curve of 1064 nm band.

As can be seen from the above figure, the reflectivity and transmittance of the wavelength of 1064 nm in the beam splitting cube were both between 40% and 50%.

As for the polarization beam splitter, a 1 inch polarization beam splitter cube was selected in this project, and the wavebands were 420–680 nm and 700–1300 nm. The polarizing beam-splitting cube reflects S light through the dielectric beam-splitting film and transmits P light, thus separating S-polarized light from P-polarized light. Extinction ratio (ER) is the ratio between the maximum transmittance and the minimum transmittance of near-perfect line incident light. When the transmission axis is parallel to the incident polarization direction, the transmission reaches the maximum; after the polarizer rotates 90, the transmission reaches the minimum [25]. The extinction ratio TP:TS of the transmitted beam of the 700~1300 nm cubic prism is greater than 1000:1. However, the average extinction ratio of 420~680 nm cube in the wavelength range is >1000:1. Their design parameters are shown in Table 3.

Table 3. Design parameters of polarization beam splitting cube in this experiment.

Design Index	Parameter
Cube size	1″ × 1″ × 1″
Texture of material	N-SF1
Transmission rate	$T_P > 90\%$
Reflectivity	$R_{S,\ Avg} > 95\%$

The transmission curve of polarization beam splitting cube is shown in Figure 10.

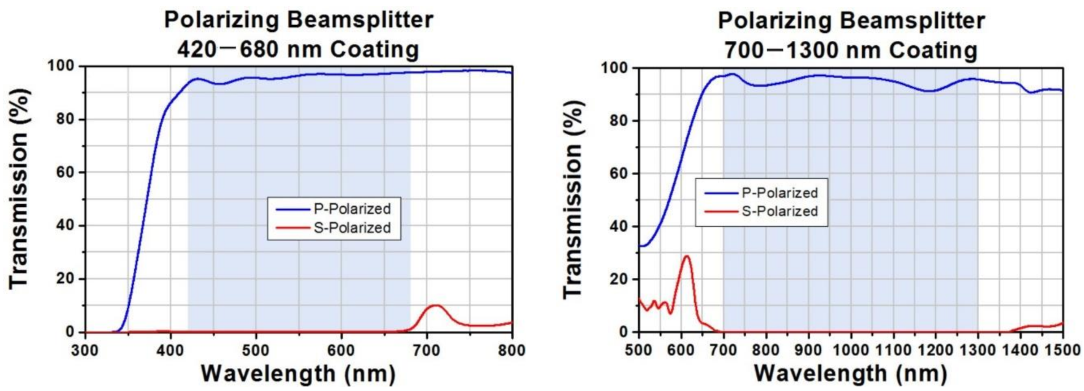

(**a**) (**b**)

Figure 10. Transmission curve of polarization beam splitting cube: (**a**) transmission rate curve of 532 nm band; (**b**) transmission rate curve of 1064 nm band.

In this experiment, an optical wave plate was also used. The optical wave plate is made of birefringent materials, and the refractive index of birefringent materials is different in the fast and slow orthogonal principal axes. The birefringence makes the light polarized along the fast axis and the slow axis of the wave plate have different propagation speeds. The refractive index of the wave plate in the fast axis direction is lower, and the light polarized along this direction travels faster, while the refractive index of the slow axis is higher, and the light speed in this polarization direction is slower [26]. When light passes through the wave plate, the speed difference causes a phase difference between two orthogonal polarization components. The actual phase difference depends on material characteristics, wave plate thickness, and signal wavelength, which can be described as

$$\Delta\Phi = \frac{2\pi d(n_1 - n_2)}{\lambda} \tag{41}$$

where $\Delta\Phi$ represents the phase difference, n_1 represents the slow axis refractive index, n_2 represents the orthogonal fast axis refractive index, d represents the wave plate thickness, and λ represents the signal wavelength.

A zero-order quarter-wave plate was used in the interferometer, composed of two multistage Shi Ying wave plates, which could produce $\lambda/4$ optical path difference. The fast axis of one wave plate is aligned with the slow axis of the other wave plate to form a composite retardation plate. The net retardation is the difference between the two wave plates, and the composite zero-order wave plate is less affected by temperature and wavelength than the multistage wave plate. The structure of the zero-order wave plate involves an etched stainless-steel washer placed between two multistage wave plates, and these three parts are bonded together with epoxy resin (epoxy resin is only coated outside the light-transmitting aperture of the wave plate). Then, the wave plate is installed in an aluminum ring which is oxidized and blackened. The shell of the aluminum ring is engraved with thin lines indicating the direction of the fast axis of the wave plate and the words of the zero-order $\lambda/4$ wave plate and design wavelength. When the incident light is linearly polarized, and the polarization plane forms 45° with the fast axis or slow axis of the wave plate, the outgoing light will become circularly polarized. If the angle between the polarization plane of linearly polarized light and the main plane is not 45°, elliptically polarized light is output. Conversely, circularly polarized light becomes linearly polarized light through the $\lambda/4$ wave plate. Its design is shown in Figure 11.

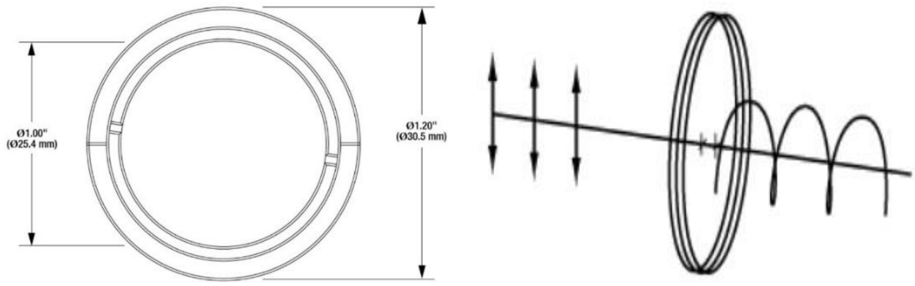

(a) (b)

Figure 11. Schematic diagram of zero-order λ/4 wave plate design: (**a**) schematic diagram of the dimension design of the zero-order λ/4 wave plate; (**b**) zero-order λ/4 wave plate model diagram.

The reflector used in the interferometer is a 1 inch broadband dielectric film plane reflector, and the reflection bands are 400–750 nm and 750–1100 nm. The reflectivity curves of these two bands are shown in Figure 12.

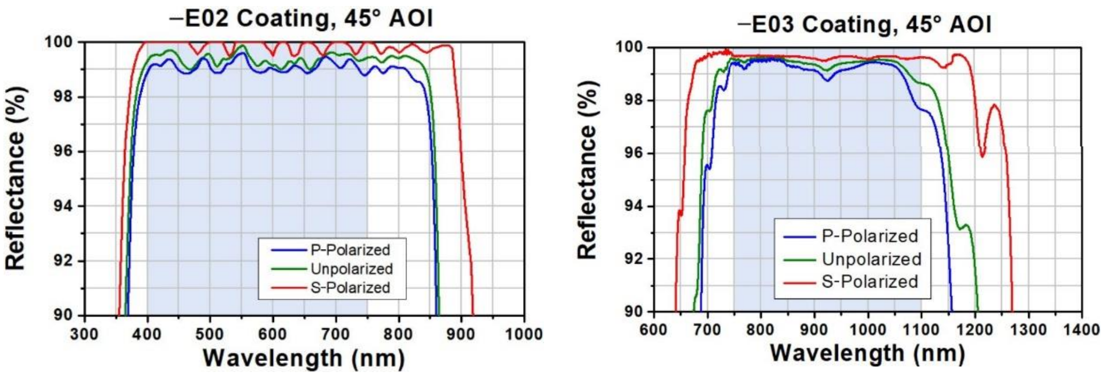

(a) (b)

Figure 12. Reflectance curve of optical mirror: (**a**) reflectance curve of 532 nm band; (**b**) reflectance curve of 1064 nm band.

Lastly, the lens used in the interferometer was a 1 inch plano-convex spherical Dan Toujing with a focal length of 30 mm. The plano-convex lens is made of N-BK7 glass, and its Abbe number is 64.17 (Abbe number represents the dispersion). The working wavelength of the V-shaped laser antireflection film is 532/1064 nm, which is used for common high-power Nd:YAG lasers with pulse output as high as 10 J/cm^2. N-BK7 is a kind of optical glass commonly used in high-power optical components. It is usually used in applications that do not need the advanced performance of ultraviolet-fused Shi Ying (such as high transmittance and low thermal expansion coefficient in ultraviolet band). For infinite and finite conjugate applications, their focal lengths are positive and have approximate optimal shapes. The plano-convex lens can converge the collimated beam on the back focus, as well as change the point light source into a collimated beam. In order to minimize spherical aberration, the collimated beam should be incident from the curved surface of the lens when focusing, and the beam emitted from the point light source should be incident from the plane of the lens when collimating. The focal length of the lens can be calculated by the simplified formula of thick lens f = R/(n − 1), where n is the refractive index and r is the radius of curvature of the convex surface of the lens. The focal length of a thick spherical lens can be calculated using the thick lens formula below [27], where n_l is the refractive index of the lens, R_1 and R_2 are the radii of curvature of surface 1 and surface 2, respectively, and D is the center thickness of the lens.

$$\frac{1}{f} = (n_1 - 1)\left[\frac{1}{R_1} - \frac{1}{R_2} + \frac{(n_1 - 1)d}{n_1 R_1 R_2}\right] \tag{42}$$

When the thick lens formula is used to calculate the focal length of a plano-convex lens, R_1 approaches infinity, and $R_2 = -R$. The negative sign before R is introduced because the sign rule of thick lens formula is deduced. Therefore, after substituting the value, the thick lens formula becomes

$$\frac{1}{f} = (n_1 - 1)\left[\frac{1}{R}\right] \tag{43}$$

The lens focal length directly calculated by the above simplified thick lens formula is the distance from the second main surface (H″) to the position of the focused spot when the collimated light is incident from the curved surface of the plano-convex lens. The position of the main surface of the thick lens can be calculated by the following formula:

$$H' = \frac{f(n_1 - 1)d}{R_2 n_1}, H'' = \frac{f(n_1 - 1)d}{R_1 n_1} \tag{44}$$

However, like the thick lens formula, h′ is simplified to 0, and h″ is simplified to

$$H'' = \frac{d}{n_1} = f - f_b \tag{45}$$

When used to calculate the principal plane position of a plano-convex lens, f_b is the back focal length of the lens, which is also often called the working distance of the lens. In the thick lens formula, the wavelength-dependent focal length of any plano-convex lens can be approximately calculated by using the refractive index of N-BK7 at the required wavelength [28]. The relationship between the refractive index of N-BK7 and wavelength is shown in Figure 13.

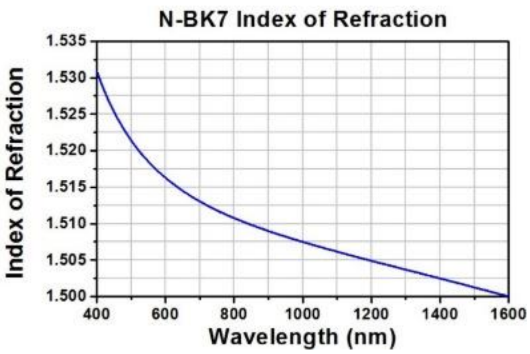

Figure 13. Refractive index of N-bk7.

The V-film on the lens surface is a multilayer dielectric antireflection film, which can obtain very small reflectivity in a narrow wavelength range. The reflectivity rises rapidly on both sides of the minimum value; thus, the reflectivity curve is V-shaped, as shown in Figure 14. The V-film has an average reflectivity of less than 0.25% on each side at the coating wavelength and is designed for an incident angle (AOI) between 0° and 20°. Compared with broadband antireflection film, V film can achieve lower reflectivity in a narrower bandwidth when AOI is specified.

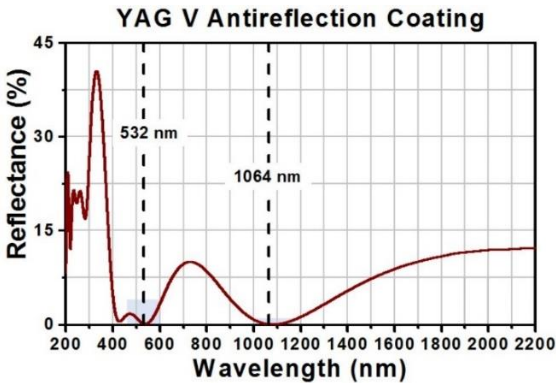

Figure 14. Reflectivity of V film.

4. Experiment

4.1. QMZ Calibration

Before processing the actual atmospheric signal, it is necessary to calibrate the MZI of four channels to determine the parameters of a_i and M_i in Equation (2). Therefore, the emitted laser after energy attenuation is introduced into the interferometer before detection, and then the integrated pulse signals on four channels are recorded for a long time. When the laser is not seeded, the emission linewidth is about 15 GHz. More than 60 longitudinal laser modes are emitted, separated by about 230 MHz, which is the free spectral range (FSR) of the laser cavity [29–32]. When the spectrum does not match the FSR (1.5 GHz) of the four-channel MZI, there will be no interference contrast. Therefore, when laser is injected into the seed light source, the interference contrast (sensitivity is 4 $\mu m \cdot K^{-1}$) with phase φ varying with optical path difference ΔOPD under the influence of temperature change is obtained. The time series of four-channel pulse signals is shown in Figure 15.

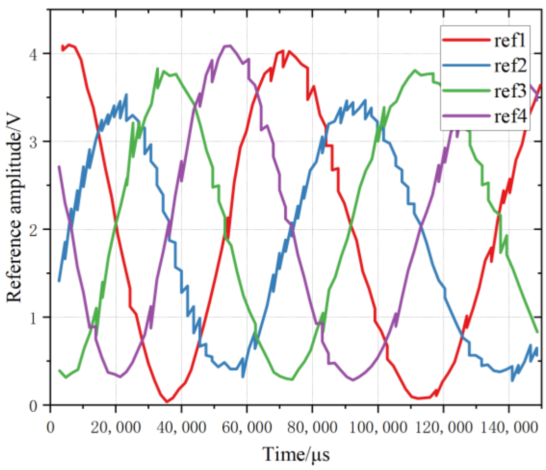

Figure 15. Signals recorded by four channels of interferometer.

Using these data as input, and fitting Equation (2) by the least square method, four coefficients M_i are determined. In order to verify the calibration accuracy, four pulse signals can be reconstructed using the determined parameters and the calculated interference phase. The result of channel 1 data is shown in Figure 16.

The calibration parameters obtained from the transmission spectrum are shown in Table 4. It can be seen that the maximum interference contrast detected by the interferometer built in this experiment is 0.869.

The correlation coefficient between the analog signal and the recorded signal is 0.9488, thus ensuring high accuracy and verifying Equation (2) and the parameters. The interference phase does not necessarily change linearly as a function of time, and the rapid signal fluctuation is well reflected in the simulation. This shows that they correspond to laser frequency fluctuation rather than measurement noise.

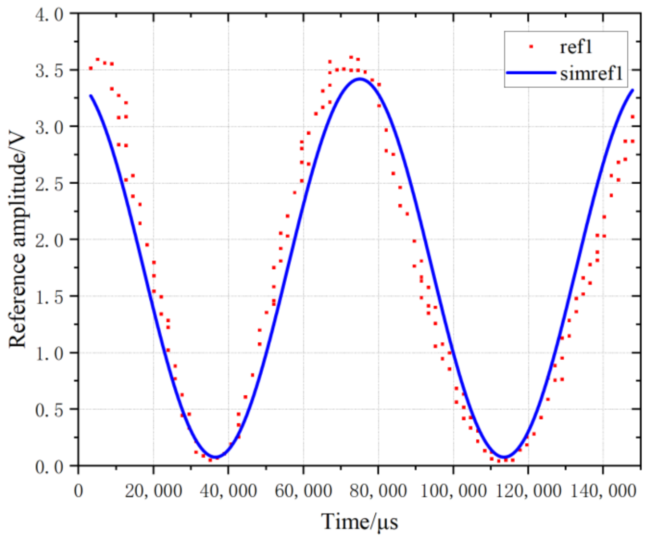

Figure 16. Comparison between recorded and simulated reference amplitudes of Channel 1.

Table 4. Measured values of channel sensitivity and interference contrast.

Sensitivity a_i		**Interference Contrast M_i**	
a_1	0.203	M_1	0.869
a_2	0.294	M_2	0.843
a_3	0.276	M_3	0.873
a_4	0.217	M_4	0.791

4.2. Acquisition of Echo Signal

The echo signal collected for the first time is shown in Figure 17. As can be seen from the figure, before 5 μs, the output signal fluctuated greatly, indicating that, at the beginning of the experiment, the echo signal was mixed with noise signal and astigmatism reflected into the interferometer.

Therefore, it is necessary to filter the noise signal and stray light entering the interferometer, and the filter of corresponding band can be added at the input end of the interferometer to ensure that the interferometer is in a dark environment during the experiment. After adjustment, the experimental result is shown in Figure 18.

4.3. Atmospheric Wind Speed Inversion Profile

The results of detector detection in the experiment are shown in Figure 19.

The inversion result is shown in Figure 20. It can be seen that the effective interference contrast of the main echo signals of channels 1 and 3 and channels 2 and 4 is close to 1, which is consistent with the theory.

The result of phase profile inversion based on echo signal data is shown in Figure 21.

The retrieved atmospheric wind speed profile in the troposphere (0–8 km) is shown in Figure 22. The experimental dataset was detected from 7:00 to 8:00 p.m. on 17 October 2022.

The weather in Shanghai on that day was as follows: sunny, northeast wind, wind direction angle of 17°, wind force of 1–2, wind speed of about 5 km/h (~1.39 m/s), all-day temperature of 12–21 °C, air pressure of 1025, rainfall of 0.0 mm, relative humidity of 52%, visibility of 25 km, and ultraviolet index of 5.

In this experiment, we should pay special attention to the fact that, when the external optical transceiver system receives the echo signal, the system is particularly sensitive to the noise signal scattered from the atmosphere and other stray light signals entering the interferometer; thus, the wind speed profile within 8 km of the above inversion may not be all true and reliable, and it is necessary to evaluate the accuracy of the measured wind speed by combining the comprehensive indicators such as the system signal-to-noise ratio (the result of the system SNR is given later). In fact, the farthest distance of wind speed detection is related to the pulse energy emitted by the large pulse laser and the overall architecture design of the system.

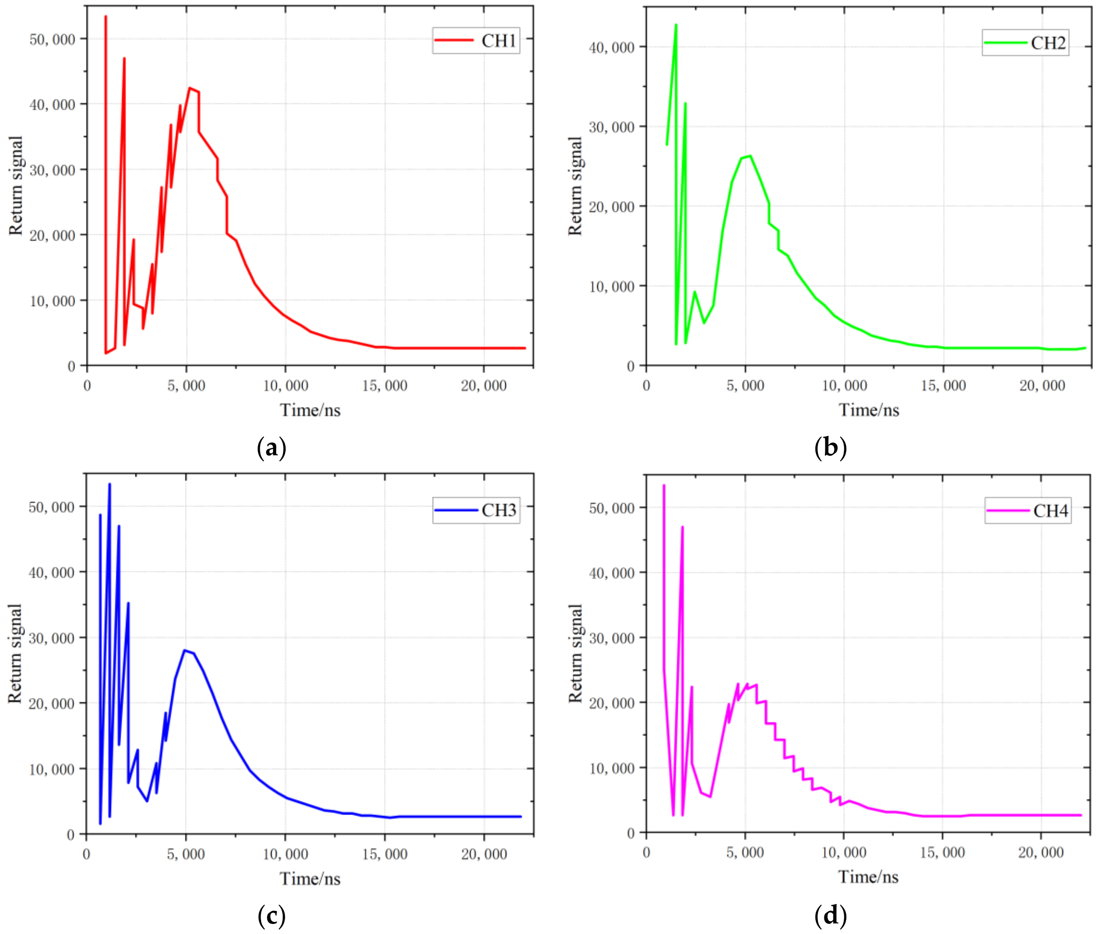

Figure 17. Original echo signal: (**a**–**d**) echo signals of each channel of the interferometer.

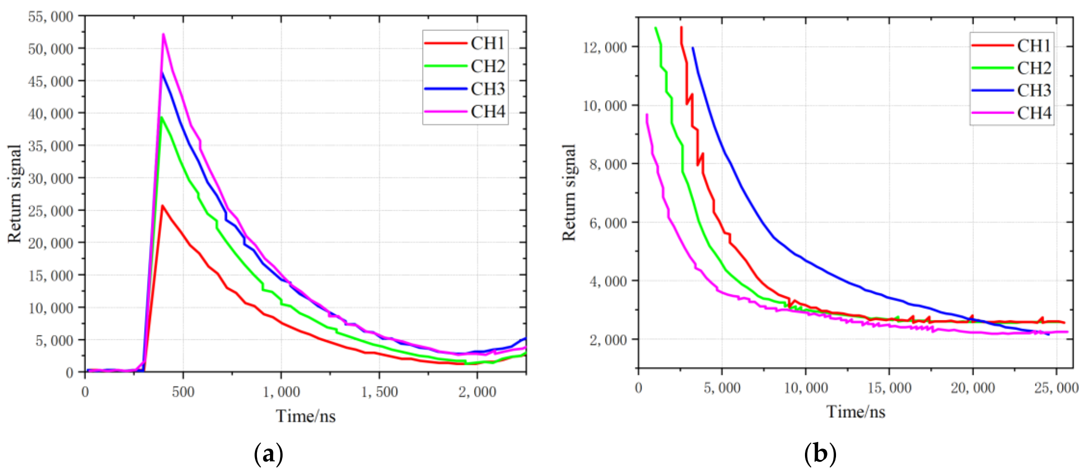

Figure 18. Filtered echo signal: (**a**) echo result graph after filtering; (**b**) result graph after eliminating overshoot.

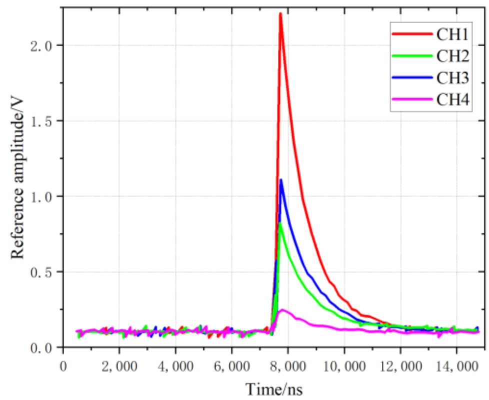

Figure 19. Measured results of detector.

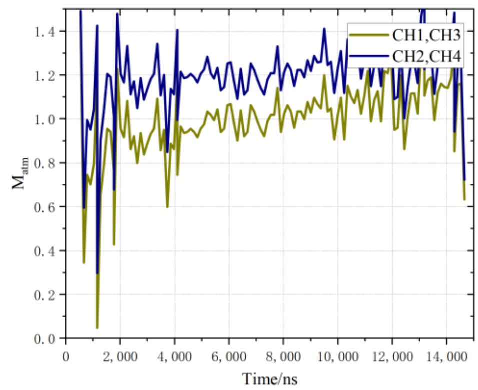

Figure 20. Inversion curve of interference contrast of main echo signal.

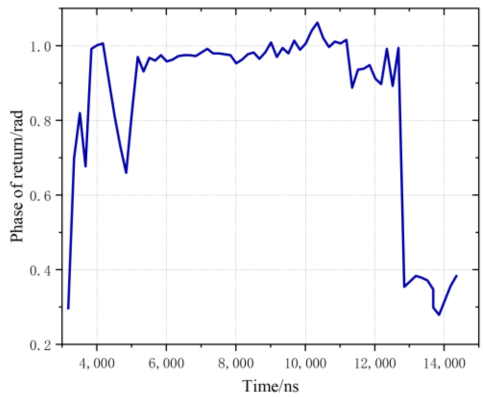

Figure 21. Inverse phase profile.

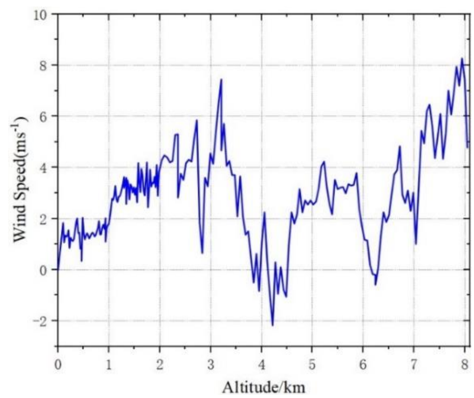

Figure 22. Inversion wind speed profile.

4.4. Temperature Detection of Troposphere Atmosphere

The atmospheric temperature T(z) is calculated from the interference contrast $M_m(\lambda,l,z)$ of the atmospheric molecule Rayleigh backscattering spectrum of the following formula and the spectral broadening γm of the atmospheric molecule Rayleigh backscattering at the height z of the scattering medium. In the formula, the speed of light is c (3×10^8 m/s), the average molecular mass is m ($28.966 \times 10^{-3}/(6.022 \times 10^{23})$ kg), the Boltzmann constant is k (1.381×10^{-23} J/K), and the wavelength is λ (532×10^{-9} m).

$$\begin{aligned} M_m(\lambda, l, z) &= \exp\left[-(\pi l \gamma_m)^2\right] \\ \gamma_m &= \frac{2\sigma_0}{c}\sqrt{\frac{2kT}{m}} \end{aligned} \tag{46}$$

The relationship between atmospheric temperature T(z) and interference contrast Mm(λ,l,z) of atmospheric molecular Rayleigh backscattering spectrum is derived below. It is calculated that $T_0 \approx 2496.98$ ($\lambda = 1064 \times 10^{-9}$ m), and $T_0 \approx 624.24$($\lambda = 532 \times 10^{-9}$ m).

$$\begin{aligned} T &= 2T_0 \ln[M_m(\lambda, l, z)] \\ T_0 &= \frac{c^2\lambda^2 m}{16\pi^2 l^2 k} \end{aligned} \tag{47}$$

The formula below shows that the absolute random error of temperature depends on the relative random error of interference contrast Mm(λ,l,z) of atmospheric molecule backscattering.

$$\mathrm{var}(T) = 2T_0 \frac{\mathrm{var}[M_m(\lambda, l, z)]}{M_m(\lambda, l, z)} \tag{48}$$

The experimental data collected by another lidar system built in the shelter laboratory (the physical part is shown in Figure 23a,b) are analyzed and extracted, and the tropospheric atmospheric temperature measurement results are shown in Figure 23c,d. The experimental dataset was detected from 7:15–9:00 p.m. on 3 January 2023. The weather in Shanghai on that day was as follows: sunny, northeast wind, wind direction angle of 66°, wind force of 3–4, wind speed of 13 km/h (~3.61 m/s), all-day temperature of 39 °C, air pressure of 1031, rainfall of 0.0 mm, relative humidity of 59%, visibility of 25 km, and ultraviolet index of 1.

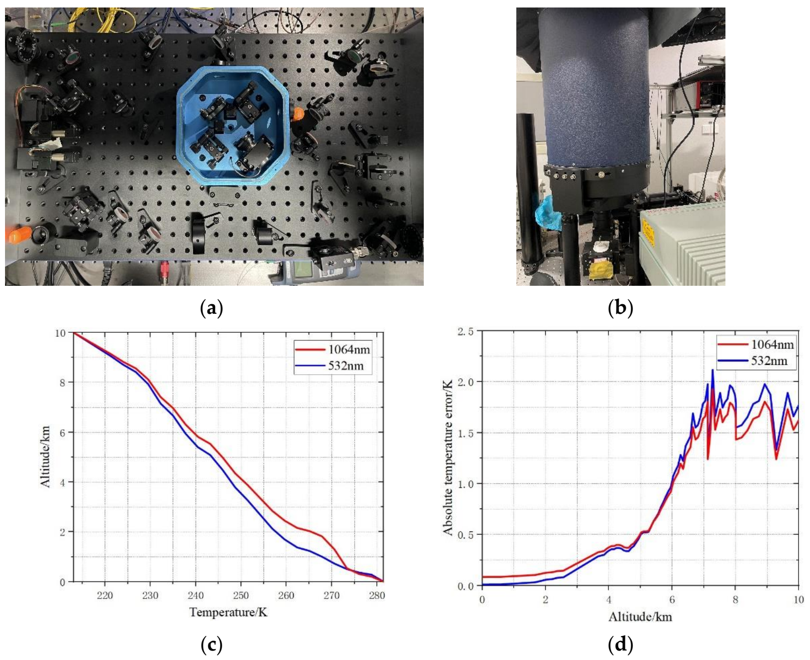

Figure 23. Inversion results of tropospheric atmospheric temperature on 3 January 2023: (**a**) physical map of part of the light path built; (**b**) receiving telescope; (**c**) temperature data under two different band experiments; (**d**) inverse temperature error profile.

5. Experimental Error Analysis

The detector detects that the interferometer output signal includes not only effective signal photons, but also background signal photons in the echo signal. Generally speaking, the background signal is superimposed on the effective signal of lidar. In practice, the measurement of background light is carried out by long-term detection and averaging; thus, compared with the error of effective signal of lidar, its error can be ignored [33]. Therefore, when calculating the wind speed measurement error, it can be assumed that the level of the background signal is measured and subtracted from the actual signal. However, the existence of background light will reduce the signal-to-noise ratio (SNR). Therefore, in the experiment, the emission power of lidar should be improved as much as possible to improve the accuracy of experimental measurement. Let N_A be the average signal photon number, N_B be the average background photon number, and η be the photon detection efficiency of the detector. Then, the signal-to-noise ratio of the system can be expressed as

$$SNR = \sqrt{\frac{\eta N_A}{1 + N_B/N_A}} \tag{49}$$

In the experiment, the signal-to-noise ratio profile of this detection is calculated according to the echo signal, as shown in Figure 24. This time, 121 data points were collected, and the transmitted pulse energy was adjusted to 255 mJ for testing. As can be seen from the figure, the signal-to-noise ratio in the range of 2 km is high, and the maximum signal-to-noise ratio can reach 1433; thus, the inverted wind speed is more accurate.

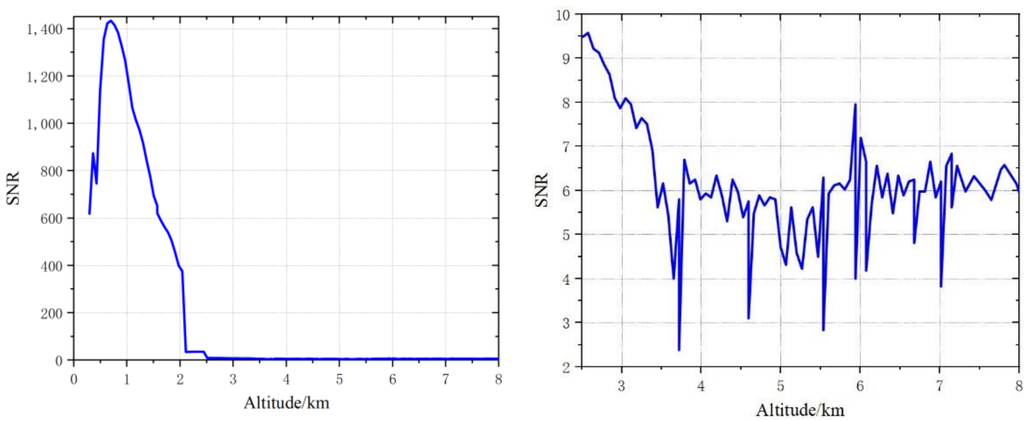

(a) (b)

Figure 24. Actual SNR of detection. (**a**) Overall diagram of system signal-to-noise ratio; (**b**) local enlarged diagram of signal-to-noise ratio over 2 km.

Therefore, with the experimental data of lidar from 7:00–8:30 p.m. on 27 October 2022, the Klett method can be used to retrieve the backscattering coefficient and extinction coefficient of atmospheric aerosol, and the retrieval result is shown in Figure 25. The weather in Shanghai on that day was as follows: light rain turned cloudy, northeast wind, wind direction angle of 68°, wind force of 1–2, wind speed of 4 km/h (~1.11 m/s), all-day temperature of 16–20 °C, air pressure of 1024, rainfall of 1.0 mm, relative humidity of 63%, visibility of 24 km, and ultraviolet index of 1.

2πl/λ represents the phase difference φ, the speed of light C is 3.0×10^8 m/s, λ is the wavelength, and the laser wavelength used in this experiment is 532 nm. L is the optical path difference, which was designed as 0.03 m in this experiment. If the signal-to-noise ratio SNR is 1000 and the value is substituted into the formula, we can get the functional relationship between the standard deviation value of wind speed measurement and the correlation coefficient F_B between the photon numbers of the four detection channels when the signal-to-noise ratio is 1000, as shown in Figure 26.

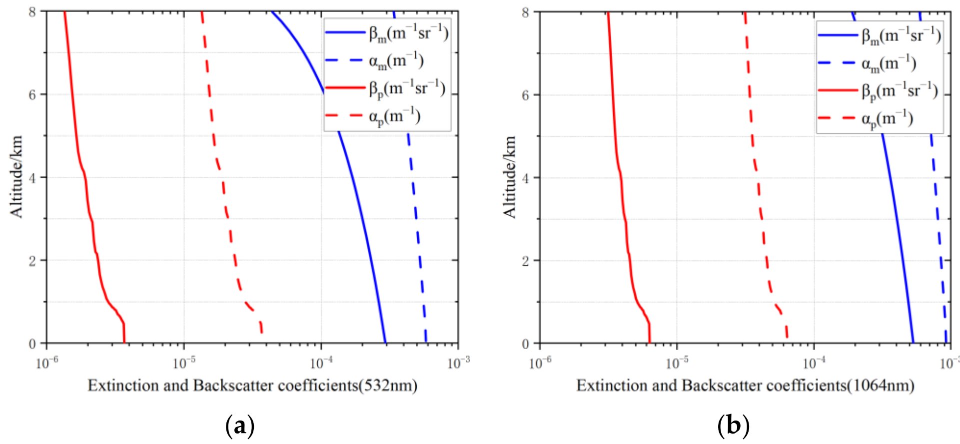

Figure 25. Inverse atmospheric backscattering coefficient and extinction coefficient: (**a**) backscattering coefficients βp, βm and extinction coefficients αp, αm of molecules and particles under the experiment of 1064 nm pulsed laser; (**b**) backscattering coefficients βp, βm and extinction coefficients αp, αm of molecules and particles under the experiment of 532 nm pulsed laser emission.

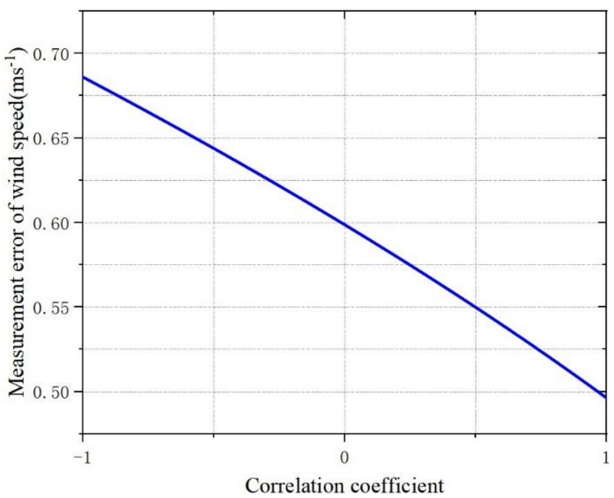

Figure 26. Relationship between wind speed measurement error and correlation coefficient between four-channel photon signals.

The coefficient D_c can be regarded as the attenuation coefficient of wind speed error. For atmosphere with a high scattering ratio, generally, $M_{atm} \approx M_{par} \approx 1$ and $M_0 \approx 1$; thus, $D_c = 1$. In clear weather, $M_{atm} \approx M_{mol} \approx 0.6$, and the attenuation factor is $D_c = 1.6$. This is inherent in the four-channel Mach–Zehnder interferometer, and the error will be reduced in the case of particle scattering. The result is shown in Figure 27.

The amplification curve of wind speed measurement error results in the range of 0 to 2 km is shown in Figure 28.

It can be seen from the figure that the actual wind measurement errors within the range of 0 to 2 km are all within 2 m/s, and the minimum error is only 0.4177 m/s, thus achieving the high-precision wind measurement goal. The core background of these experiments is to debug the interferometer, put the interferometer in the working state of frequency discrimination, and accurately capture the frequency difference between the echo signal and the transmitted signal, which is the key to the success of the experiment. The working temperature of the instruments purchased in this project is between −10 °C and 50 °C, which is not suitable for experiments in an extreme temperature environment. In addition, the interferometer is also extremely sensitive to temperature changes, and the interferometer must be kept in a dust-free and constant-temperature environment. If the ambient temperature of the interferometer changes obviously, it is necessary to recalibrate the interferometer and strictly discuss the influence of temperature change on the experiment.The experimental results are given in Table 5.

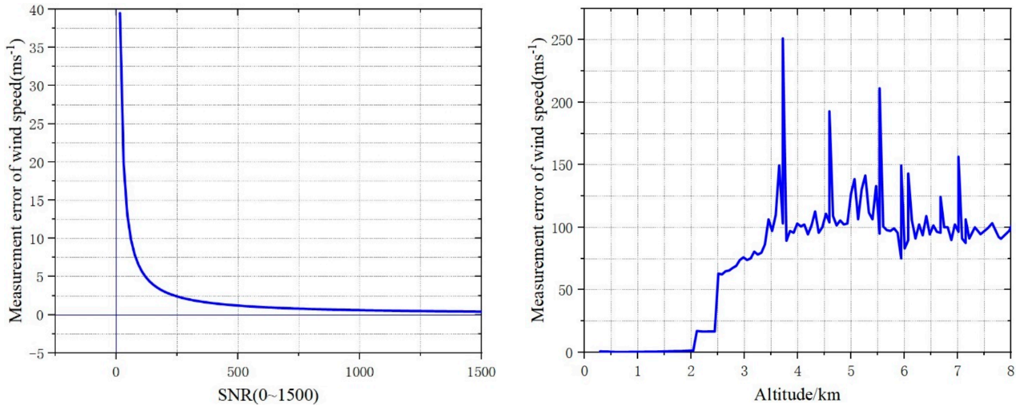

(**a**) (**b**)

Figure 27. Wind speed measurement error result chart: (**a**) diagram showing the relationship between wind speed measurement error and signal-to-noise ratio; (**b**) result chart of wind speed measurement error and detection range.

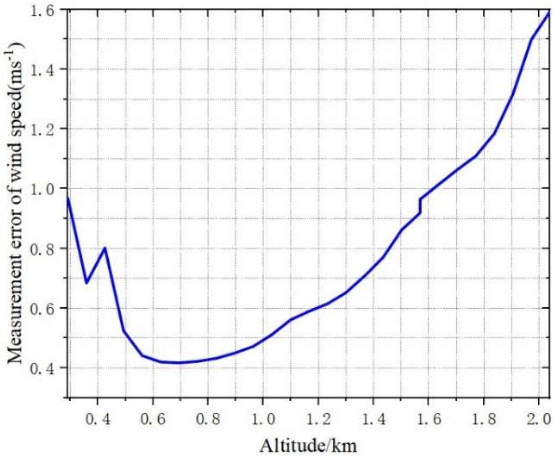

Figure 28. Local enlargement of wind speed error.

Table 5. Relationship among laser emission energy, SNR, and effective detection height.

Parameter	Result
Monopulse energy	1200 mJ
Maximum emission energy	255 mJ
Maximum SNR	1433 (@maximum emission energy)
Wind speed detection range	0–8 km
Effective wind speed detection range	0–2 km
Accuracy of wind speed measurement	1.6 m·s^{-1} (@H = 2 km)
Effective measurement range of atmospheric molecules and aerosols	0–8 km
Atmospheric temperature detection range	0–8 km
Measurement accuracy of extinction coefficient of aerosol	±0.001 m^{-1}
Accuracy of atmospheric temperature measurement	±2 K

6. Conclusions

Doppler wind lidar has always been the main method to solve the problems of atmospheric wind field detection, which can provide wind field profile data for meteorological dynamics research and numerical weather forecasting. The most important is the spectral frequency discriminator, and the accuracy of the frequency discriminator can directly affect the accuracy of wind speed detection. This paper discusses the research background of atmospheric wind field detection and introduces in detail the main research methods of atmospheric wind field detection, as well as the existing research on wind lidar. Furthermore, the basic theory of Doppler wind lidar based on a four-channel Mach–Zehnder interferometer was systematically analyzed, and the principle and performance evaluation of this system were analyzed in detail. In addition, the emission mechanism of large pulse laser was studied in detail. The ground-based observation experiment was carried out using the Doppler anemometry lidar designed in this paper, the echo signal of the atmospheric troposphere in Hongkou District was accurately obtained, and the radial atmospheric wind speed profile was inversed according to the theoretical model. The maximum interference contrast detected by the interferometer built in this experiment was 0.869, and the correlation coefficient between the analog signal and recorded signal was 0.9488. The experimental results showed that the maximum signal-to-noise ratio (SNR) of the system could reach 1433 when the emission pulse energy of the large pulse laser was adjusted to 255 mJ, and the farthest wind speed detection distance was about 8 km. The high-precision wind speed detection range could reach 2 km, and the actual wind measurement errors in this range were all within 1.593 m/s, while the minimum error was only 0.418 m/s. In addition, the backscattering coefficient and extinction coefficient of atmospheric molecules and aerosols in the range of 8 km and the atmospheric temperature in the range of 10 km were also measured. The measurement accuracy of aerosol extinction coefficient was $\pm 0.001\ \mathrm{m}^{-1}$, and the measurement error of atmospheric temperature within 10 km was within 2 K, which achieving the expected goals.

With the continuous progress of Doppler lidar wind measurement technology, the wind measurement radar system will develop toward integration and multifunctionality. The method studied in this paper can still be improved. The atmospheric parameters and lidar system components can be modeled to simulate the echo signals of lidar systems in different bands under different meteorological conditions, and the influence of air pollution and bad weather on the detection accuracy of the system can be analyzed. The design of the wind speed inversion algorithm and data acquisition system can be optimized to improve the denoising performance of the system. Further optimizing the actual emission energy of the large pulse laser can increase the actual effective detection distance. The data can be compared and analyzed in different scenes such as day, night, and polluted weather, and the influence of temperature on interferometer frequency discrimination can be further considered. In addition, future experiments can discuss the structural characteristics of the high-density urban boundary layer [34], such as surface morphology, thermal instability, and the influence of land/sea wind, detect the vertical wind profiles of upwind, urban area, and downwind in the city, compare the vertical wind profiles of wind tunnel, mesoscale simulation, and lidar, and estimate the benefits of Doppler wind lidar for short-term low-level wind ensemble forecasts [35].

Author Contributions: Conceptualization, J.L. (Jun Li) and Y.L.; methodology, H.Y.; software, Z.L.; validation, J.L. (Jun Li), Y.L. and H.Y.; formal analysis, J.L. (Jin Liu); investigation, J.Q.; resources, H.Y.; data curation, Y.C.; writing—original draft preparation, Y.L.; writing—review and editing, Y.L.; visualization, J.L. (Jun Li); supervision, H.Y.; project administration, H.Y.; funding acquisition, H.Y. All authors have read and agreed to the published version of the manuscript.

Funding: This research was funded by the Key Laboratory of Space Active Opto-electronics Technology of the Chinese Academy of Sciences (2021ZDKF4), the Shanghai Science and Technology Innovation Action Plan (22dz1201300), and the Joint Astronomical Fund of the National Natural Science Foundation of China (U1831133).

Institutional Review Board Statement: Exclude this statement.

Informed Consent Statement: Exclude this statement.

Data Availability Statement: Data sharing not applicable. No new data were created or analyzed in this study. Data sharing is not applicable to this article. Data underlying the results presented in this paper are not publicly available at this time but may be obtained from the authors upon reasonable request.

Conflicts of Interest: The authors declare no conflict of interest.

Appendix A. Signal Processing and Noise-Dependent Measurement Errors

Appendix A.1. Signal Processing

In this appendix, we refer to BP03 to recall expressions of errors of atmospheric wind speed and attenuated backscatter coefficients using a QMZ interferometer. Let us start with the optical lidar signal S_{atm} (in number of photons) at the QMZ input as follows:

$$S_{atm}(R) = S_{mol}(R) + S_{par}(R) = \frac{EAT_{inst}}{hv} \int_{r=R-\delta R/2}^{r=R+\delta R/2} \frac{\left(\beta_{mol}(r) + \beta_{par}(r)\right)}{r^2} T_{atm}^2(r) dr \quad \text{(A1)}$$

where E is the emitted energy, A is the telescope area, $Tinst$ is the instrumental (emission and reception) transmission, hv is the emission photon energy, R is the range, and $T_{atm}(r) = \exp\left[-\int_0^r \left(\alpha_{mol}(r') + \alpha_{par}(r')\right) dr'\right]$, where the mol and par subscripts are related to the molecular and particulate scattering, respectively.

The signal delivered by each channel of the A-CCD outputs (in photoelectrons), for i = 1 to 4, can be written as follows:

$$S_i = \frac{S_{tot}}{4} a_i \left[1 + M_i M_{atm} \sin\left(\varphi + (i-1)\frac{\pi}{2}\right)\right] + S_{bi} \quad \text{(A2)}$$

where a_i is the relative photometric efficiency of channel i with $\sum_{i=1}^4 a_i = 4$, and M_i is the intrinsic modulation of channel i. S_{bi} is the background signal due to solar detected light and A-CCD intrinsic noise. As all the photons incident on the MZI arrive on the detectors, we have the following:

$$S_{tot} = \frac{4}{\sum_{i=1}^4 M_i^{-1}} \sum_{i=1}^4 \frac{(S_i - S_{bi})}{a_i M_i} = \eta S_{atm} \quad \text{(A3)}$$

where η is the mean quantum efficiency of the detectors, φ is the interference phase, and M_{atm} is the atmospheric effective interference modulation given by the molecular and particulate atmospheric backscattered signals as follows:

$$M_{atm} = \frac{M_{par}(R_\beta - 1) + M_{mol}}{R_\beta} \quad \text{(A4)}$$

where the lidar scattering ratio R_β is defined by the ratio of the total to the molecular backscatter coefficients as

$$R_\beta = \frac{\beta_{mol} + \beta_{par}}{\beta_{mol}}$$

Depending on the scattering ratio, the atmospheric modulation coefficient M_{atm} varies between M_{mol} and M_{par}, representing the interference modulations given by pure molecular and particulate signals, respectively. After subtraction of the background, the four signals are combined two-by-two in order to produce a complex signal Q (with in-phase and quadrature components) as follows:

$$Q = Q_2 + iQ_1,$$

$$Q = Q_2 + iQ_1,$$

$$Q_1 = \frac{a_3(S_1 - S_{b1}) - a_1(S_3 - S_{b3})}{a_3M_3(S_1 - S_{b1}) + a_1M_1(S_3 - S_{b3})}$$

$$Q_2 = \frac{a_4(S_2 - S_{b2}) - a_2(S_4 - S_{b4})}{a_4M_4(S_2 - S_{b2}) + a_2M_2(S_4 - S_{b4})} \tag{A5}$$

The interference phase, φ, is obtained by the argument of the complex signal Q as follows:

$$\varphi = \arg(Q) \tag{A6}$$

Subtracting the reference phase φ_r, obtained in the same way on a highly attenuated pick-up of the laser emission, one can obtain the line-of-sight (LOS) particle velocity V_LOS as follows:

$$V_{LOS} = \frac{c\lambda}{4\pi\Delta}(\varphi - \varphi_r) \tag{A7}$$

where Δ is the MZI optical path difference, λ is the operating wavelength, and c is the light celerity in vacuum. Using this differential approach, V_LOS can be obtained in the whole measurement range $\pm$ c$\lambda/(4\Delta)$ without the need for locking the emitting frequency with the interference phase. The atmospheric modulation is obtained by the modulus of Q divided by the modulus of the reference signal as follows:

$$M_{atm} = \frac{|Q|}{|Q_r|} \tag{A8}$$

One can see, from Equation (A3), that, once M_mol and M_par are determined, M_atm gives access to the scattering ratio R_β:

$$R_\beta = \frac{M_{par} - M_{mol}}{M_{par} - M_{atm}} \tag{A9}$$

Separated molecular and particulate signals can be obtained (with the same instrumental constant) using the following:

$$S_{mol} = \frac{M_{par} - M_{atm}}{M_{par} - M_{mol}}\frac{S_{tot}}{\eta};\ S_{par} = \frac{M_{atm} - M_{mol}}{M_{par} - M_{mol}}\frac{S_{tot}}{\eta} \tag{A10}$$

However, this step is not necessary for the retrieval of the particulate backscatter and extinction coefficients, which can be obtained as follows:

$$\beta_{par} = \beta_{mol}(R_\beta - 1) = \beta_{mol}\frac{M_{atm} - M_{mol}}{M_{par} - M_{atm}} \tag{A11}$$

The total particulate optical depth over the vertical column can be derived from the total signal and the scattering ratio as follows:

$$\tau_{par} = \frac{1}{2}\ln\left(\frac{R_\beta\beta_{mol}}{r^2S_{tot}}\right) - \tau_{mol} \tag{A12}$$

One way to determine the particulate extinction coefficient is to derive Equation (A12), which gives the particulate optical depth with altitude z as follows:

$$\alpha_{par} = \frac{1}{2}\frac{d}{dr}\left(\ln\left(\frac{R_\beta\beta_{mol}}{r^2S_{tot}}\right)\right) - \alpha_{mol} \tag{A13}$$

which allows us to remove the need for calibration. This method is sensitive to noise, and other ways to derive extinction can provide better results. We, however, use this conservative approach for the sake of simplicity.

Appendix A.2. Preliminary Evaluation of M_{par} and M_{mol}

Assuming Gaussian spectral profiles, the two interference modulations M_{mol} and M_{par} can be expressed as a function of the optical path difference Δ and the 1/e linewidth (expressed in wavenumber) of the related spectral functions of atmospheric scattering convolved by the laser emitted width, as given in BP03, such that

$$M_s = \exp\left[-(\pi\gamma_s\Delta)^2\right] \tag{A14}$$

where s stands for *mol* or *par*. For the particle scattering, γ_{par} is defined as a first approximation by the laser source linewidth γ_{las}. Assuming γ_{las} on the order of 3×10^{-3} cm^{-1} (or 100 MHz, corresponding to the transform limit of a 3 ns pulse), we see that we obtain $\gamma_{\text{par}}\Delta \approx 10^{-2}$ and $M_{\text{par}} \approx 1$ for an OPD value of 3 cm. We, thus, remain in the case of a high contrast for the particulate signal, with some margin on the laser linewidth. For the molecular scattering, mol is dominated by the thermal molecular velocity as follows:

$$\gamma_{mol} = \frac{2}{\lambda c}\sqrt{\frac{2kT}{m}} \tag{A15}$$

which is about 7×10^{-2} cm^{-1}, implying that $\gamma_{\text{mol}}.\Delta \approx 0.2$ and $M_{\text{mol}} \approx 0.6$ for an OPD of 3 cm.

Appendix A.3. Noise-Dependent Statistical Error

We give here the random error depending on the detected noise. Assuming, for simplicity, that all the relative sensitivities a_i are equal to 1 and that all the instrumental modulations M_i are equal to M_0, the standard deviation of VLOS is given in BP03 as follows:

$$\sigma(V_{LOS}) = \frac{c\lambda}{4\pi\Delta}\frac{\sqrt{2}}{SNR}\frac{\sqrt{1-\frac{1}{2}F_B M_0^2 M_{atm}^2 \sin^2(2\varphi)}}{M_0 M_{atm}} \tag{A16}$$

where SNR is the signal-to-noise ratio, and F_B is a correlation coefficient among the four detection channels given by $F_{\text{B}} = (S_{tot} - S_b)/(S_{tot} + S_b)$, where S_{tot} is the number of signal photoelectrons, and S_b is the total number of photo-electrons of the radiative and detection background (both summed with the weighting factors given in Equation (A3)). We also assume here that the background can be measured over an extended range gate and subtracted for any measurement pixel with a negligible impact on bias and SNR. This assumes that the background noise is taken with a much higher SNR than the atmospheric signal. For accurate measurements, the SNR needs to be high; thus, we have $S_{\text{tot}} >> S_{\text{b}}$ and $F_B \approx 1$, leading to a minimum square root factor.

If, as we propose, the laser frequency is not locked to the interferometer, the phase can take any value between 0 and 2π. Thus, for the performance assessment of the instrument, we average the error on φ and obtain the following:

$$\sigma(V_{LOS}) = \frac{c\lambda}{4\pi\Delta}\frac{\sqrt{2}}{SNR}\frac{1}{M_0 M_{atm}}\sqrt{1-\frac{M_0^2 M_{atm}^2}{4}} \tag{A17}$$

The factor $D_c = \frac{1}{M_0 M_{atm}}\sqrt{1-\frac{M_0^2 M_{atm}^2}{4}}$ can be seen as a degradation factor on the wind error due to the contrasting degradation. For high scattering ratios, we have $M_{\text{atm}} \approx M_{\text{par}} \approx 1$; assuming a perfect MZI, we have $M_0 \approx 1$, such that $D_c = 1.0$. In clear air, for which we have $M_{\text{atm}} \approx M_{\text{mol}} \approx 0.6$, the degradation factor is $D_c \approx 1.6$. This is intrinsic to the QMZ technique, for which error is reduced in presence of particle scattering.

The relative standard deviation of the statistical error on R_β is linked to the error on modulus of Q (Equation (A8)). After averaging over φ, it can be expressed as follows (BP03):

$$\frac{\sigma(R_\beta)}{R_\beta} = \frac{\sqrt{2}}{SNR}\frac{R_\beta}{M_0(M_{par}-M_{mol})}\sqrt{1-\frac{3}{4}F_B M_0^2 M_{atm}^2} \tag{A18}$$

We can then derive the error on β_{par} as follows:

$$\sigma(\beta_{par}) = \frac{\sqrt{2}}{SNR}\frac{R_\beta(\beta_{par}+\beta_{mol})}{M_0(M_{par}-M_{mol})}\sqrt{1-\frac{3}{4}F_B M_0^2 M_{atm}^2} \tag{A19}$$

The error on the particulate extinction coefficient is given (after averaging over φ) as follows:

$$\sigma(\alpha_{par}) = \frac{1}{\sqrt{2}\delta r}\frac{1}{SNR}\sqrt{1+\frac{2R_\beta^2}{M_0^2(M_{par}-M_{mol})^2}\left(1+\frac{3}{4}F_B M_0^2 M_{atm}^2\right)-\frac{R_\beta M_{atm}}{M_{par}-M_{mol}}(1+F_B)} \tag{A20}$$

References

1. Abedin, M.N.; Bradley, A.T.; Sharma, S.K.; Misra, A.K.; Lucey, P.G.; McKay, C.P.; Ismail, S.; Sandford, S.P. Mineralogy and astrobiology detection using laser remote sensing instrument. *Appl. Opt.* **2015**, *54*, 7598–7611. [CrossRef] [PubMed]
2. Mohanakumar, K.; Kottayil, A.; Anandan, V.K.; Samson, T.; Thomas, L.; Satheesan, K.; Rebello, R.; Manoj, M.G.; Varadarajan, R.; Santosh, K.R.; et al. Technical Details of a Novel Wind Profiler Radar at 205 MHz. *J. Atmospheric Ocean. Technol.* **2017**, *34*, 2659–2671. [CrossRef]
3. Liu, Z.; Barlow, J.F.; Chan, P.-W.; Fung, J.C.H.; Li, Y.; Ren, C.; Mak, H.W.L.; Ng, E. A Review of Progress and Applications of Pulsed Doppler Wind LiDARs. *Remote Sens.* **2019**, *11*, 2522. [CrossRef]
4. Song, M.; Wang, Y.; Mamtimin, A.; Gao, J.; Aihaiti, A.; Zhou, C.; Yang, F.; Huo, W.; Wen, C.; Wang, B. Applicability Assessment of Coherent Doppler Wind LiDAR for Monitoring during Dusty Weather at the Northern Edge of the Tibetan Plateau. *Remote Sens.* **2022**, *14*, 5264. [CrossRef]
5. Smith, J.A.; Chu, X. Investigation of a field-widened Mach–Zehnder receiver to extend Fe Doppler lidar wind measurements from the thermosphere to the ground. *Appl. Opt.* **2016**, *55*, 1366. [CrossRef] [PubMed]
6. Wolken-Möhlmann, G.; Bischoff, O.; Gottschall, J. Analysis of wind speed deviations between floating lidars, fixed lidar and cup anemometry based on experimental data. *J. Phys. Conf. Ser.* **2022**, *2362*, 012042. [CrossRef]
7. Wang, L.; Gao, F.; Wang, J.; Yan, Q.; Chang, B.; Hua, D. Design and experimental verification of a novel Mie Doppler wind lidar based on all-fiber Mach-Zehnder frequency discriminator. *Opt. Commun.* **2016**, *389*, 5–9. [CrossRef]
8. Zhou, Y.; Li, L.; Wang, K.; Zhang, X.; Gao, C. Coherent Doppler wind lidar signal denoising adopting variational mode decomposition based on honey badger algorithm. *Opt. Express* **2022**, *30*, 25774–25787. [CrossRef]
9. Cañadillas, B.; Beckenbauer, M.; Trujillo, J.J.; Dörenkämper, M.; Foreman, R.; Neumann, T.; Lampert, A. Offshore wind farm cluster wakes as observed by long-range-scanning wind lidar measurements and mesoscale modeling. *Wind. Energy Sci.* **2022**, *7*, 1241–1262. [CrossRef]
10. Jiang, P.; Yuan, J.; Wu, K.; Wang, L.; Xia, H. Turbulence Detection in the Atmospheric Boundary Layer Using Coherent Doppler Wind Lidar and Microwave Radiometer. *Remote Sens.* **2022**, *14*, 2951. [CrossRef]
11. Witschas, B.; Vieitez, M.O.; van Duijn, E.J.; Reitebuch, O.; van de Water, W.; Ubachs, W. Spontaneous Rayleigh–Brillouin scattering of ultraviolet light in nitrogen, dry air, and moist air. *Appl. Opt.* **2010**, *49*, 4217–4227. [CrossRef] [PubMed]
12. Kidambi Sekar, A.P.; van Dooren, M.F.; Rott, A.; Kühn, M. Lower Order Description and Reconstruction of Sparse Scanning Lidar Measurements of Wind Turbine Inflow Using Proper Orthogonal Decomposition. *Remote Sens.* **2022**, *14*, 2681. [CrossRef]
13. Cheng, Z.; Liu, D.; Zhang, Y.; Yang, Y.; Zhou, Y.; Luo, J.; Bai, J.; Shen, Y.; Wang, K.; Liu, C.; et al. Field-widened Michelson interferometer for spectral discrimination in high-spectral-resolution lidar: Practical development. *Opt. Express* **2016**, *24*, 7232–7245. [CrossRef] [PubMed]
14. Misaka, T.; Nakabayashi, F.K.; Obayashi, S.; Inokuchi, H. Filtering Algorithm of Airborne Doppler Lidar Measurements for Improved Wind Estimation. *Trans. Jpn. Soc. Aeronaut. Space Sci.* **2015**, *58*, 149–155. [CrossRef]
15. Gräfe, M.; Pettas, V.; Cheng, P.W. Wind field reconstruction using nacelle based lidar measurements for floating wind turbines. *J. Phys. Conf. Ser.* **2022**, *2265*, 042022. [CrossRef]
16. Smith, J.A.; Chu, X. Exploration of Whole Atmosphere Lidar: Mach-zehnder Receiver to Extend Fe Doppler Lidar Wind Measurements from the Thermosphere to the Ground. *EPJ Web Conf.* **2016**, *119*, 12004. [CrossRef]
17. Viselli, A.; Faessler, N.; Filippelli, M. LiDAR Measurements of Wind Shear Exponents and Turbulence Intensity Offshore the Northeast United States. *J. Offshore Mech. Arct. Eng.* **2022**, *144*, 042001. [CrossRef]
18. Kliebisch, O.; Uittenbosch, H.; Thurn, J.; Mahnke, P. Coherent Doppler wind lidar with real-time wind processing and low signal-to-noise ratio reconstruction based on a convolutional neural network. *Opt. Express* **2022**, *30*, 5540–5552. [CrossRef]
19. Cheng, Z.; Liu, D.; Luo, J.; Yang, Y.; Zhou, Y.; Zhang, Y.; Duan, L.; Su, L.; Yang, L.; Shen, Y.; et al. Field-widened Michelson interferometer for spectral discrimination in high-spectral-resolution lidar: Theoretical framework. *Opt. Express* **2015**, *23*, 12117–12134. [CrossRef]
20. Tang, S.; Li, T.; Guo, Y.; Zhu, R.; Qu, H. Correction of various environmental influences on Doppler wind lidar based on multiple linear regression model. *Renew. Energy* **2022**, *184*, 933–947. [CrossRef]

21. Dai, H.; Gao, C.; Lin, Z.; Wang, K.; Zhang, X. Wind lidar signal denoising method based on singular value decomposition and variational mode decomposition. *Appl. Opt.* **2021**, *60*, 10721–10726. [CrossRef]
22. Kim, J.Y.; Kim, M.S. A comparison of offshore met-mast and lidar wind measurements at various heights. *J. Korean Soc. Coast. Ocean. Eng.* **2017**, *29*, 12–19. [CrossRef]
23. Ma, Y.; Zhu, Y.; Liu, B.; Li, H.; Jin, S.; Zhang, Y.; Fan, R.; Gong, W. Estimation of the vertical distribution of particle matter (PM2.5) concentration and its transport flux from lidar measurements based on machine learning algorithms. *Atmos. Chem. Phys.* **2021**, *21*, 17003–17016. [CrossRef]
24. Tucker, S.C.; Weimer, C.; Hardesty, R.M. The Athena-OAWL Doppler Wind Lidar Mission. *EPJ Web Conf.* **2016**, *119*, 1002. [CrossRef]
25. Filimonov, P.A.; Ivanov, S.E.; Gorodnichev, V.A.; Belov, M.L.; Fedotov, Y.V. Measurements of Wind Speed and Direction with an Aerosol UV Lidar. *Atmos. Ocean. Opt.* **2021**, *34*, 443–446. [CrossRef]
26. Liu, D.; Zhao, T.; Boiyo, R.; Chen, S.; Lu, Z.; Wu, Y.; Zhao, Y. Vertical Structures of Dust Aerosols over East Asia Based on CALIPSO Retrievals. *Remote Sens.* **2019**, *11*, 701. [CrossRef]
27. Yuan, J.; Wu, K.; Wei, T.; Wang, L.; Shu, Z.; Yang, Y.; Xia, H. Cloud Seeding Evidenced by Coherent Doppler Wind Lidar. *Remote Sens.* **2021**, *13*, 3815. [CrossRef]
28. Cremons, D.R.; Abshire, J.; Allan, G.; Sun, X.; Riris, H.; Smith, M.; Guzewich, S.; Yu, A.; Hovis, F. Development of a Mars lidar (MARLI) for measuring wind and aerosol profiles from orbit. In Proceedings of the Lidar Technologies, Techniques, and Measurements for Atmospheric Remote Sensing XIV, Berlin, Germany, 11–12 September 2018.
29. Yang, S.; Peng, F.; von Löwis, S.; Petersen, G.N.; Finger, D.C. Using Machine Learning Methods to Identify Particle Types from Doppler Lidar Measurements in Iceland. *Remote Sens.* **2021**, *13*, 2433. [CrossRef]
30. Daniel, M.; Carey, N. LiDAR for Wind Measurement. *Sea Technol.* **2019**, *60*, 10–13.
31. Mahdizadeh, A.; Tofighi, E.; Schmid, R. Comparison between the NMPC and EOR control of wind turbines using LIDAR wind measurements. *J. Physics: Conf. Ser.* **2018**, *1037*, 032046. [CrossRef]
32. Hristova-Veleva, S.; Zhang, S.Q.; Turk, F.J.; Haddad, Z.S.; Sawaya, R.C. Assimilation of DAWN Doppler wind lidar data during the 2017 Convective Processes Experiment (CPEX): Impact on precipitation and flow structure. *Atmos. Meas. Tech.* **2021**, *14*, 3333–3350. [CrossRef]
33. Angelou, N.; Mann, J.; Dellwik, E. Scanning Doppler lidar measurements of drag force on a solitary tree. *J. Fluid Mech.* **2021**, *917*, A30. [CrossRef]
34. He, Y.; Ren, C.; Mak, H.W.L.; Lin, C.; Wang, Z.; Fung, J.C.H.; Li, Y.; Lau, A.K.H.; Ng, E. Investigations of high-density urban boundary layer under summer prevailing wind conditions with Doppler LiDAR: A case study in Hong Kong. *Urban Clim.* **2021**, *38*, 100884. [CrossRef]
35. Nomokonova, T.; Griewank, P.J.; Löhnert, U.; Miyoshi, T.; Necker, T.; Weissmann, M. Estimating the benefit of Doppler wind lidars for short-term low-level wind ensemble forecasts. *Q. J. R. Meteorol. Soc.* **2022**, *149*, 192–210. [CrossRef]